N-cadherin dynamically regulates pediatric glioma cell migration in complex environments

Running title: N-cadherin dynamically regulates glioma migration

Dayoung Kim[1], James M Olson[2,3] and Jonathan A Cooper[1]*

1 Basic Sciences Division, Fred Hutchinson Cancer Center, Seattle, WA, 98109, USA

2 Clinical Division, Fred Hutchinson Cancer Center, Seattle, WA, 98109, USA

3 Ben Towne Center for Childhood Cancer Research, Seattle Children's Research Institute, Seattle, WA, 98101, USA

Summary

Pediatric gliomas invade the brain by migrating between nerve cells or exploiting extracellular matrix along blood vessels. This research reveals cross-talk between YAP1/TAZ signaling and N-cadherin that regulates leader-follower cell phenotypes and migration efficiency in neural and extracellular matrix environments.

Abstract

Pediatric high-grade gliomas are highly invasive and essentially incurable. Glioma cells migrate between neurons and glia, along axon tracts, and through extracellular matrix surrounding blood vessels and underlying the pia. Mechanisms that allow adaptation to such complex environments are poorly understood. N-cadherin is highly expressed in pediatric gliomas and associated with shorter survival. We found that inter-cellular homotypic N-cadherin interactions differentially regulate glioma migration according to the microenvironment, stimulating migration on cultured neurons or astrocytes but inhibiting invasion into reconstituted or astrocyte-deposited extracellular matrix. N-cadherin localizes to filamentous connections between migrating leader cells but to epithelial-like junctions between followers. Leader cells have more surface and recycling N-cadherin, increased YAP1/TAZ signaling, and increased proliferation relative to followers. YAP1/TAZ signaling is dynamically regulated as leaders and followers change position, leading to altered N-cadherin levels and organization. Together, the results suggest that pediatric glioma cells adapt to different microenvironments by regulating N-cadherin dynamics and cell-cell contacts.

Keywords pediatric brain tumor, pediatric high-grade glioma, cell-cell adhesion, collective migration, leader cell, endocytosis, N-cadherin, YAP1

*Correspondence: jcooper@fredhutch.org

Introduction

Pediatric high-grade gliomas (PHGGs) and diffuse midline gliomas (DMGs) resemble adult glioblastoma (GBM) in being aggressively invasive and essentially incurable, but differ in having fewer oncogenic mutations and arising in the growing brains of children (Azzarelli et al., 2018; Jones et al., 2012). Invasion occurs along a variety of routes, with cells moving individually, as collective strands, or as multicellular networks between neuronal and glial cell bodies, along white matter tracts, and through extracellular matrix (ECM)-rich spaces under the leptomeninges and around blood vessels (Alieva et al., 2019; Cuddapah et al., 2014; Gritsenko et al., 2012; Kluiver et al., 2020; Neve et al., 2017; Osswald et al., 2015). The varied invasion routes and dynamic morphologies of migrating glioma cells, including branching migration, locomotion and translocation, resemble those of migrating neural progenitors and immature neurons during brain development, suggesting that similar molecular mechanisms may be at play (Beadle et al., 2008; Cuddapah et al., 2014; Venkataramani et al., 2022; Zarco et al., 2019). Molecular and phenotypic profiling reveals multiple tumor subclones with distinct invasive capacity that cooperate in vitro (Vinci et al., 2018), but the molecular and cellular mechanisms contributing to invasion in different microenvironments are poorly understood.

The ability of glioma cells to migrate either between other cells or through ECM implies differential regulation of cell-cell and cell-matrix adhesion (Wu et al., 2021). Intercellular adhesion between glioma cells may allow them to coordinate their movements during collective invasion, while glioma cell adhesion to normal cells may aid invasion into the brain parenchyma (Collins and Nelson, 2015; Friedl and Mayor, 2017; Gritsenko et al., 2020; Ng et al., 2012). The complex invasion routes and plasticity between individual and collective migration implies that glioma cells can adapt to making contacts with ECM, normal cells or other tumor cells, but the specific molecules involved are unknown.

The cell-cell adhesion molecule N-cadherin (*CDH2*, N-cad) is upregulated in approximately 60-80% of adult glioblastomas and is associated with increased mortality (Gravendeel et al., 2009; Noh et al., 2017). High N-cad expression is also associated with poor overall survival in all types of pediatric brain cancer (Fig. S1 A). During normal development, N-cad is critical both to maintain cell-cell adhesion in the neuroepithelium and also to stimulate single-cell migration of neural progenitors and neural crest cells (Ganzler-Odenthal and Redies, 1998; Hatta and Takeichi, 1986; Jossin and Cooper, 2011; Kadowaki et al., 2007; Kawauchi et al., 2010; Kon et al., 2019; Theveneau et al., 2010; Vassilev et al., 2017; Xu et al., 2001). Thus N-cad has the potential to regulate single-cell or collective migration in gliomas.

At the molecular level, N-cad is a transmembrane receptor. Extracellular homophilic interactions between N-cad molecules on adjacent cells can bind cells together or repel them through contact inhibition of locomotion (Scarpa et al., 2015). Surface N-cad also functions cell-autonomously to regulate other transmembrane receptors, such as the fibroblast growth factor receptor (FGFR) and integrins (Collins and Nelson, 2015; Kon et al., 2019; Mui et al., 2016; Nguyen et al., 2019). Inside the cell, the N-cad cytoplasmic domain interacts with p120-catenin, β-catenin and α-catenin. The catenins link N-cad to the actin cytoskeleton and regulate N-cad traffic through the endosomal recycling pathway. Unbound cadherins are rapidly endocytosed and recycled (Le et al., 1999; Reynolds and Roczniak-Ferguson, 2004). N-cad recycling is important during astrocyte migration to replace surface N-cad at the cell front (Peglion et al., 2014). Catenins also regulate cell migration through Rho GTPases and Wnt signaling (Harris and Peifer, 2005; Reynolds and Roczniak-Ferguson, 2004; Vassilev et al., 2017).

In this study we report that N-cad inhibits PHGG cell migration on ECM but stimulates migration on neurons or astrocytes, consistent with glioma-glioma cell interactions slowing migration while glioma-neural cell interactions speed migration. N-cad is localized and regulated differently in PHGG leader and follower cells during migration. N-cad localizes to filamentous connections that join leader cells to each other and to adjacent neurons. In contrast, follower cells are tightly packed, forming linear, epithelial-like N-cad junctions with their neighbors. The leader cells have higher cell proliferation and nuclear localization of the transcription coactivator Yes-associated protein 1 (YAP1) as well as increased surface N-cad, when compared with follower cells. YAP1 nuclear localization is determined by cell density and its activation increases N-cad surface level and recycling. Thus, YAP1 activation at the migration front increases N-cad surface levels, promoting collective migration and invasion in neural environments.

Results

N-cad inhibits PHGG migration on ECM but stimulates migration on neural cells.

We investigated the migration properties of five PHGG and DMG cell lines by transferring tumor spheroids to different environments designed to mimic invasion through the ECM or neural cells (neuron or astrocyte). All cell lines migrated collectively, with very few single cells. Even as cells spread away from the spheroid, they remained connected, suggesting an important role for cell-cell adhesion molecules. Curiously, migration in ECM environments did not correlate with migration over neurons. For example, one MYC-N amplified PHGG line, PBT-05, migrated faster on neurons but slower on laminin or reconstituted basement membrane (Matrigel) than the transcriptionally similar PBT-04 line (Fig. S1, B-D). We hypothesized that this paradoxical migration behavior might result from altered expression of cell adhesion molecules. N-cad is the most highly expressed cell-cell adhesion molecule at the RNA level in most PHGG lines (Brabetz et al., 2018) (Fig. S1 E and Table S 1) and was readily detected at the protein level in the three DMG and two PHGG lines that we analyzed (Fig. S1 F). Interestingly, N-cad is more highly expressed in PBT-05 than PBT-04 cells, correlating with migration on neurons but inversely correlating with migration on ECM.

To directly test whether N-cad differentially regulates migration in different environments, we established PBT-05 lines expressing control or N-cad shRNA and characterized them by Western blot and RNASeq. N-cad shRNA inhibited N-cad expression at the protein level (Fig. S1 G) and RNA level (7-fold decrease, Fig. S1 H). Expression of other cadherins was unaffected except for CDH3 (2.8-fold increase, Fig. S1 H and Table S2). Importantly, integrin expression was also unaffected. N-cad depletion did not affect spheroid formation or DNA synthesis (Fig. S1, I-K) but stimulated migration on laminin and invasion into Matrigel (Fig. 1, A-D, Video 1 and Fig. S1, N-O). Migration on laminin was also stimulated by transient knockdown of N-cad with siRNA (Fig. S1, L-M). Thus, N-cad inhibits migration on ECM. In contrast, migration on cultured cerebellar neurons or mouse astrocytes was inhibited by N-cad depletion (Fig. 1, E-H and S1 P). Astrocyte cultures secrete a 3D ECM scaffold mimicking the brain parenchyma (Gritsenko and Friedl, 2018). To test whether N-cad depletion inhibits glioma migration on astrocyte cultures through glioma cell interactions with astrocyte cells or ECM, we used decellularized astrocyte cultures. N-cad depletion stimulated migration on astrocyte-derived, decellularized ECM, suggesting that N-cad stimulates glioma migration on astrocyte cells but not ECM (Fig. 1, I-J and S1 Q). These results show that N-cad differentially regulates migration according the environment, increasing migration on neural cells (neurons or glia) but inhibiting migration on ECM (laminin, Matrigel or astrocyte-derived ECM).

N-cad also regulated the balance between collective and individual cell migration. In ECM or neural cell environments, N-cad depletion increased the number of PBT-05 cells that migrate individually away from the collective and decreased the number of contacts between cells at the migration front (Fig. 2, A-C and S1, N-O). The remaining connections at the migration front were elongated and resembled the filamentous junctions or tumor microtubes that connect cell networks in adult glioblastoma (Fig. 2 B, arrowhead) (Osswald et al., 2015; Venkataramani et al., 2022). Quantification of individual cell movements revealed that N-cad depletion decreased glioma cell directionality on neurons but increased directionality on laminin, without significantly affecting the average migration speed in either environment (Fig. 2, D-I). These findings suggest that N-cad promotes collective relative to single-cell migration in multiple environments but has environment-specific effects on cell migration directionality and overall speed, stimulating directionality and overall distance migrated in neural and astrocyte environments while inhibiting directionality and overall migration and invasion into ECM.

N-cad stimulates and inhibits migration through intercellular homotypic interaction.

At the molecular level, N-cad can regulate cell migration through multiple mechanisms, including intercellular N-cad homotypic interactions, cell-autonomous regulation of receptor kinases, and intracellular catenin signaling (Khalil and de Rooij, 2019; Kon et al., 2019; Theveneau et al., 2010; Vassilev et al., 2017). We wondered whether intercellular N-cad homotypic interactions might explain its conflicting roles in migration in different environments. For example, neurons or glia ahead of the migration front might increase directionality and stimulate overall migration, while other glioma cells behind the migration front might decrease directionality and inhibit overall migration. This model predicts that N-cad makes glioma-neuron junctions as well as glioma-glioma junctions. Indeed, we detected N-cad in filamentous contacts between migrating PBT-05 cells and cerebellar neurons (Fig. 3 A). To test whether intercellular N-cad contacts were important for migration, we expressed a mutant that is incapable of forming strand-swapped homotypic dimers, $\text{Ncad}^{\text{W161A}}$ (Shapiro et al., 1995; Tamura et al., 1998). $\text{Ncad}^{\text{W161A}}$ and Ncad^{WT} were tagged with mCherry and expressed at similar level (Fig. 3 B). $\text{Ncad}^{\text{W161A}}$ expression mimicked N-cad depletion, inhibiting cell migration on neurons but stimulating migration on laminin (Fig. 3, C-D and S2, A-B), consistent with intercellular homotypic interactions stimulating and inhibiting migration in different environments. To directly test whether N-cad in the environment stimulates migration, we assayed migration on a surface coated with the N-cad extracellular domain (ECD). Glioma cells migrated rapidly on N-cad ECD, dependent on endogenous N-cad (Fig. 3 E). Moreover, glioma cells migrated poorly over N-cad-depleted astrocytes (Fig. 3, F-G and S2 C). Together, these findings suggest that intercellular N-cad homotypic interactions with neural cells ahead of the migration front speed overall migration, while interactions with other glioma cells behind the migration front slow overall migration (Fig. 3 H).

Catenins regulate N-cad surface levels to stimulate or inhibit migration.

Cadherins and catenins reciprocally co-regulate: cadherins localize catenins to the membrane while catenins regulate cadherin surface retention and internalization, cytoskeletal linkage, and signaling (Harris and Tepass, 2010; Katsuno-Kambe and Yap, 2020; Nanes et al., 2012; Reynolds and Roczniak-Ferguson, 2004). We tested whether catenins regulate N-cad expression or surface levels in PHGG and their effect on migration. Depletion of p120-, β- or α-catenin individually had little effect on the steady-state protein levels of other catenins or of N-cad (Fig. 4, A-B). However, in each case, the steady-state level of N-cad on the cell surface was reduced (Fig. 4, C-D). Remarkably, catenin depletion increased cell migration on laminin and inhibited migration on astrocytes, in parallel with the N-cad surface level (Fig. 4, E-F and S2, D-E). These findings suggest that catenins stimulate or inhibit glioma cell migration in different environments primarily by regulating N-cad surface levels.

To test whether N-cad regulates catenin protein levels or localization, we investigated catenin expression and localization in control and N-cad-depleted cells. Western blotting showed that N-cad depletion significantly decreased the level of β- but not α- or p120-catenin and induced a mobility shift in p120-catenin, possibly indicating a change in phosphorylation state (Reynolds and Roczniak-Ferguson, 2004) (Fig. S2, F-G). We used immunofluorescence to localize N-cad and catenins in mixed cultures of control and N-cad-depleted cells. In control cells, N-cad and all three catenins co-localized on the plasma membrane (Fig. S2 H, arrowheads), with additional localization of N-cad, β- and α- but not p120-catenin in perinuclear vesicles (Fig. S2 H, arrows). In cells lacking N-cad (dashed regions in Fig. S2 H), both the surface and vesicular localization of β- and α-catenin was decreased, while p120-catenin decreased at the surface and increased in the cytoplasm consistent with release during endocytosis (Davis et al., 2003). Overall, these findings are consistent with N-cad regulating catenin localization, while catenins regulate N-cad surface levels with corresponding effects on cell migration.

Altered cell contacts and increased N-cad levels, endocytosis and recycling at the migration front.

Studies of cancer invasion suggest that “leader cells” at the migration front and the bulk of “follower cells” are functionally distinct, and that cooperation between leaders and followers increases overall migration (Konen et al., 2017; Zhang et al., 2019). We noted that N-cad localizes to distinct cell-cell contacts between PHGG leaders and followers: radially oriented, neurite-like, filamentous cell-cell contacts between leaders (white arrowheads, Fig. 5 A, r2, see also Fig. 2 B), and circumferential, epithelial-like, contacts between follower cells (yellow arrowheads, Fig. 5 A, r1) but forms. Filamentous N-cad junctions also link leader cells to neurons (Fig. 3 A). These structures appear to be similar to filamentous junctions or tumor microtubes that form between infiltrating adult glioblastoma cells (Gritsenko et al., 2020; Osswald et al., 2015). We also noted that leading cells contain more N-cad perinuclear vesicles (white arrow, Fig. 5 A, r2) compared with follower cells, even though the number of transferrin receptor-containing vesicles is the same (Fig. 5 B). Intracellular N-cad vesicles colocalized extensively with early endosomes (Rab5), at intermediate levels with recycling endosomes (Rab11), and poorly with lysosomes (LAMP1) or the Golgi (GM130), suggesting that N-cad endocytosis and recycling may be increased in leader relative to follower cells, with possible functional significance for migration (Fig. 5, C-D).

To test whether N-cad endocytosis is regulated differently in leaders and followers, we used an antibody uptake assay. Migrating cells were cooled to 4 °C and incubated with antibody to the N-cad extracellular domain. Unbound antibody was removed, and cells were transferred to 37 °C for different times. Cells were fixed and surface and internalized N-cad antibodies were detected using two different fluorochrome-conjugated secondary antibodies (Fig. S3 A). Initially, most N-cad antibody was on the surface but over time it progressively entered perinuclear endosomes that stained for early endosome markers EEA1 and Rab5 and recycling markers Rab4 and Rab11 (Fig. 5 E and S3, B-C). Quantification showed that leader cells internalized more N-cad antibody than followers (Fig. 5, F). With longer incubation, more N-cad antibody returned to the surface of leaders than followers implying more recycling (Fig. S3 D). Indeed, a modified assay confirmed that more N-cad antibody recycled to the surface in leader than follower cells (Fig. 5 G and S3, E-F). Together, these results show that leader cells internalize and recycle more N-cad antibody than followers. However, we noted that leader cells also bound more N-cad antibody initially (Fig. 5 E). This implies increased surface, internal and therefore total N-cad protein levels. Increased N-cad protein was unexpected since we show below that N-cad RNA is equal in leader and follower cells.

We took two approaches to test whether N-cad protein levels are actually higher in leader than follower cells. First, migrating cells were fixed, permeabilized, stained with N-cad antibody and imaged, and fluorescence intensity was integrated across multiple *z* sections. Total N-cad intensity was significantly higher in leaders than followers (Fig. 5 H). Second, we measured surface N-cad levels in leader and follower cells by flow cytometry (Fig. S3 G-K). PBT-05 cells were transduced to express Dendra2, a photoconvertible fluorescent protein, fused to histone-2B. Cell nuclei of leader and follower cells were irradiated to photoconvert histone H2B-Dendra2 from green to red (leaders) or yellow (followers) (Fig. S3, G-H). Cells were then released from the plate without use of proteases (to avoid cleaving N-cad), labeled with N-cad antibody, and N-cad intensity in leader and follower cells was measured by flow cytometry (Fig. S3, I-K). N-cad surface levels were significantly higher in leader than follower cells.

Together, the evidence suggests that distinct N-cad cell-cell junctions form between migrating PHGG leader and follower cells, and these distinct junctions correlate with increased total, surface and endosomal levels of N-cad protein in leader cells. However, it is unclear whether the altered N-cad levels, subcellular distribution, and cell junctions are a cause or consequence of cell position in the migratory stream and the types of cell contacts formed.

Altered proliferation, YAP1/TAZ signaling, and gene expression of leader cells.

In light of the altered N-cad protein levels and distribution in PHGG leaders and followers, we performed additional phenotypic characterization. Leader cells from epithelial-derived cancers such as breast and lung carcinomas express different genes and proliferate more slowly than followers (Konen et al., 2017; Zhang et al., 2019). To test whether PHGG leaders and followers also proliferate differently, we pulse-labeled migrating cells with EdU (Buck et al., 2008). EdU incorporation was significantly higher in leader than follower cells whether migrating on laminin or neurons or invading Matrigel (Fig. 6, A-B). Thus, unlike the situation in breast and lung cancer, PHGG leader cells are more, not less, proliferative than followers.

YAP1 and TAZ (*WWTR1*) are related transcriptional coactivators that are regulated by cell density and stimulate cell proliferation, plasticity and migration (Panciera et al., 2017; Totaro et al., 2018; Zanconato et al., 2019). YAP1 and TAZ are nuclear in sub-confluent cells but excluded from the nucleus in dense cultures, mediated in part by signals from cadherins (Kim et al., 2011; Panciera et al., 2017). PHGG leader cells are less crowded and proliferate faster than followers, suggesting that YAP1/TAZ signaling may be activated. Indeed, YAP1 was nuclear in a higher proportion of leader than follower PBT-05 cells, regardless of whether the cells were migrating in Matrigel, laminin or neurons (Fig. 6, C-D). Nuclear localization of YAP1 was also higher in leader than follower cells in DMG lines PBT-24 and PBT-29 (Fig. S4, A-B), suggesting that YAP1 nuclear localization may be a common feature of leader cells during pediatric glioma migration.

We tested used RNA sequencing to compare gene expression in leader and follower cells that we isolated by photoconversion and flow cytometry, as described above (Fig. S3, G-I). Only 44 gene transcripts increased and 36 decreased more than $2^{0.5}$-fold in leaders relative to followers out of 19,729 genes that were quantified (Benjamini-Hochberg adjusted *p*-value < 0.05, four independent experiments) (Table S3). Expression of N-cad, catenins, other junctional regulators, and YAP1 and TAZ was unchanged (Fig. S4 C). However, expression of YAP-response genes, CTGF, CYR61, ACTA2, GADD45A and CDKN1A, and wound-healing genes TNFRSF12A, CD9, TPM1, ANXA1 and ANXA5, was higher in leader than follower cells (Fig. 6 E and Table S3). Gene ontology analysis suggested a modest increase in wound healing and stress gene signatures (Fig. S4 D). This suggests that YAP1-signaling and wound-healing gene expression is increased in leader cells and may contribute to their faster migration and higher proliferation.

Leader and follower cells are not predetermined

Leader cells may be genetically or epigenetically predetermined and selected to lead invasion based on, for example, increased expression of pro-migratory genes. Alternatively, cell phenotypes may be plastic, with leader cell properties induced by the unique environment at the migration front (Khalil and de Rooij, 2019; Konen et al., 2017; Zhang et al., 2019). To better understand whether the PHGG leader phenotype is predetermined or plastic, we photoconverted histone H2B-Dendra2-expressing leader cells and monitored their positions as migration continued (Fig. 6, F-G and Video 2). Regardless of migration conditions – neurons, laminin or Matrigel – 40-60% of leader cells were overtaken by cells from behind during the time it took to move 35-40 µm (Fig. 6 H). Furthermore, YAP1 was nuclear in cells that had recently transitioned to become leaders and cytoplasmic in cells that had recently become followers (Fig. 6 I). These findings show that leader and follower cells change position during migration and invasion, suggesting they are not predetermined. Moreover, YAP1 signaling and gene expression (Fig. S4, C-D) change as leaders and followers switch position.

YAP1 regulation by cell density independent of N-cad

We tested whether reduced cell density or reduced N-cad engagement increases YAP1 nuclear translocation in leader cells. First, we imaged YAP1 in migrating N-cad-depleted cells (Fig. 7 A). Leader nuclei contained more YAP1 than followers regardless of N-cad expression level. This suggests that N-cad does not directly regulate YAP1 nuclear localization. Second, we tried to equalize leader and follower exposure to environmental N-cad by observing cells migrating over N-cad ECD (Fig. 7, B-C). YAP1 was still largely nuclear in leader cells and cytoplasmic in followers. This result aligns with nuclear localization of YAP1 in leader cells migrating on neurons (Fig. 6, C-D). Third, to test the role of cell crowding, control or N-cad-depleted cells were plated on a micropatterned coverslip to generate cell clusters of different sizes. The proportion of cells with nuclear YAP1 decreased as cluster size increased, consistent with larger clusters having more center cells and fewer edge cells, and hence more cell-cell contact, regardless of N-cad status (Fig. 7, D-E). Additionally, N-cad antibody uptake decreased as nuclear YAP1 decreased in large clusters, showing that there is a correlation between YAP1 and N-cad internalization (Fig. 7 F). This suggests that YAP1 is excluded from the nucleus in follower cells by cell crowding, independent of N-cad, and translocates to the nucleus of leader cells, even if there N-cad is present in the surrounding environment, because cells are less crowded.

YAP1/TAZ signaling regulates cell migration and N-cad protein levels.

YAP1/TAZ signaling stimulates cell migration and invasion in other systems (Panciera et al., 2017; Totaro et al., 2018; Zanconato et al., 2019). The increased YAP1 nuclear localization and increased expression of YAP-response genes in leader cells may stimulate their migration. We tested whether YAP1/TAZ signaling regulates PHGG cell migration using YAP1 and TAZ siRNA. Overall migration was inhibited by single knockdown of either YAP1 or TAZ and further inhibited by knockdown of YAP1 and TAZ together (Fig. S5, A-B). YAP1/TAZ depletion also inhibited PBT-05 migration in basal media where potential confounding effects of YAP1/TAZ signaling on cell proliferation are minimized (Fig. S5 B). This suggests that the increased YAP1/TAZ signaling in leader cells may promote overall migration.

YAP1/TAZ signaling regulates cell-cell junctions and cadherin turnover in other systems, such as during vascular development (Kim et al., 2017; Neto et al., 2018). Therefore, we tested whether YAP1/TAZ signaling regulates N-cad levels or trafficking in PHGG. We quantified N-cad immunofluorescence intensity using sparse cultures, where YAP1 is nuclear. N-cad total and surface intensities were decreased in YAP1/TAZ-depleted cells (Fig. 8, A-F). Moreover, YAP1/TAZ depletion inhibited surface N-cad antibody binding in leader cells (where YAP1 is active) but not follower cells (where YAP1 is inactive) (Fig. 8, G-H), resulting in decreased N-cad antibody internalization (Fig. S5, C-D). As a control, transferrin surface level and uptake were independent of YAP1/TAZ expression (Fig. 8 F and S5, E-F). Together, these findings suggest a model in which decreased crowding of leader cells leads to N-cad-independent nuclear translocation of YAP1 and expression of migration genes. Elevated nuclear YAP1 also increases N-cad surface levels and recycling in leader cells, which promotes migration in neural environments but inhibits migration on ECM (Fig. 8 I).

Discussion

Our results suggest that N-cad differentially regulates glioma cell migration in neural cell or ECM environments in vitro, with higher N-cad level increasing migration on neurons and astrocytes and lower levels increasing migration in ECM. Thus, the level of N-cad might determine the choice of migration routes in vivo, switching between invading the gray matter and axon tracts as opposed to the ECM around blood vessels and under the pia. We also found that migrating leader and follower cells are phenotypically different. Leader cells are connected by N-cad-dependent filamentous junctions, have high levels of surface and recycling N-cad, and increased YAP1/TAZ signaling and proliferation, compared with followers. These phenotypes of leader and follower cells are not stable and leaders and followers exchange during migration or invasion. Thus, pediatric glioma cells adapt to their surroundings to optimize migration.

Both the pro-migratory and anti-migratory effects of N-cad on cell migration depended on homotypic N-cad binding to N-cad in the environment or other cells. In addition, α-, β- and p120-catenins inhibited migration in ECM and stimulated migration on neural cells, as expected if their main role is to stabilize N-cad on the surface to increase homotypic binding. A simple hypothesis is that leader cell migration is stimulated by N-cad engagement on the leading edge and slowed by N-cad engagement on the trailing edge (Fig. 3 H). Leading edge stimulation predominates in neural environments but trailing edge inhibition predominates in ECM. This could be explained simply by physical force vectors, but signaling mechanisms may also play a role. For example, N-cad engagement can locally inhibit focal adhesions (Camand et al., 2012; Julich et al., 2015). N-cad can locally inhibit Rac and activate Rho to repress protrusion and induce cell polarization and contact-inhibition of locomotion (Ouyang et al., 2013; Scarpa et al., 2015; Theveneau et al., 2010). Surface N-cad can also regulate heterologous receptors on the same cell, such as stabilizing the FGFR during cortical neuron migration (Kon et al., 2019). Internalized catenins may also regulate directional migration of glial and endothelial cells (Vassilev et al., 2017). In our system, however, surface N-cad appears to both stimulate and inhibit migration through homotypic binding or signaling interactions between cells.

N-cad surface levels and recycling were higher in leader than follower cells. N-cad recycling is needed for migration in many systems, including cortical neuron migration during development (Kawauchi et al., 2010), Xenopus neural crest (Kuriyama et al., 2014) and various cancer cells (Gritsenko et al., 2020; Sandilands et al., 2023; Wint et al., 2023). N-cad recycling may help disassembly and reassembly of different types of cell-cell junctions, allowing the migrating cells to rearrange and cooperate for overall migration. Collective migration and metastasis are more efficient for cancer cells with weak cell-cell adhesions (partial EMT) than when cell-cell adhesions are completely disrupted (full EMT) (Saxena et al., 2020; Te Boekhorst and Friedl, 2016; Wu et al., 2021). Thus N-cad endocytosis and recycling may allow to migrating glioma cells to reorganize filamentous connections between leader cells into tighter junctions between followers.

While leader and follower cells are predetermined in breast and lung cancer (Konen et al., 2017; Zhang et al., 2019), migrating glioma leader and follower cells switched positions, even when confined in ECM. Such switching has been observed in various biological processes, including embryonic development and cancer invasion (Cai et al., 2014; Jakobsson et al., 2010; Khalil and de Rooij, 2019; Zhang et al., 2019). In this leader-follower interchange, cells maintain cell-cell contact but continually rearrange and form different types of adhesions. For example, endothelial tip cells have serrated VE-cad junctions, high VE-cad turnover and low cell-cell cohesion, and switch positions with follower cells that have straight, continuous VE-cad junctions, low turnover and high cell-cell cohesion (Bentley et al., 2014). VE-cad turnover is regulated by YAP1 during vascular development (Neto et al., 2018). Similarly, the distinct N-cad distribution we observe between leader and follower glioma cells could facilitate the leader-follower interchange. Moreover, YAP1 translocates to the nucleus when cells reach the migration front, independent of N-cad but dependent on cell density. YAP1 in turn regulates N-cad level and trafficking, implying that YAP1 might contribute to the leader-follower interchange and phenotypic plasticity.

The mechanisms by which YAP1 regulates N-cad levels and trafficking remain to be explored. YAP1 is widely expressed in human brain tumors and strongly associated poor survival (Orr et al., 2011). Leader cells expressed higher levels of YAP1-response and wound-healing gene transcripts, but transcript levels of N-cad and proteins known to regulate cadherin traffic, such as p120-catenin (Davis et al., 2003), Rab5/11 (Kawauchi et al., 2010) and Rac1 (Akhtar and Hotchin, 2001), were similar. Therefore, N-cad is likely regulated at the level of protein synthesis or turnover. More endosomal N-cad recycled to the surface of leader than follower cells, implying that follower cells might divert more N-cad for lysosomal degradation, but our attempts to interfere with N-cad endocytosis or degradation specifically were unsuccessful. Further understanding of the mechanism and function of N-cad recycling for glioma cell migration will require cargo-specific ways to selectively regulate endocytosis and recycling.

Cancer cells exhibit a remarkable plasticity in cytoskeletal and adhesion properties that enable adaptation to varied microenvironments encountered during invasion and metastasis (Te Boekhorst and Friedl, 2016; Wu et al., 2021). This plasticity is particularly evident in adult and pediatric gliomas, which rapidly spread by invading through different brain regions (Alieva et al., 2019; Cuddapah et al., 2014; Gritsenko et al., 2012; Kluiver et al., 2020; Neve et al., 2017; Osswald et al., 2015). Our results suggest that N-cad mediates the switch between collective or single-cell migration and allows pediatric glioma cells to adapt to their environment. YAP1/TAZ signaling is dynamically regulated as leaders and followers change position, leading to altered N-cadherin levels and organization. YAP1/TAZ inhibition may result in reduced migratory capacity without substantially reducing tumor bulk, culminating in disease control but not eradication.

Materials and methods

Cells

Human PHGG cell lines PBT-05 and PBT-04 cells and human DMG cell lines PBT-22, PBT-24 and PBT-29 were a kind gift from James Olson (Seattle Children's Research Institute). PHGG and DMG cells were maintained in glioma growth medium (Human NeuroCult NS-A Proliferation kit (Stemcell Technologies, 05751) supplemented with 20 ng/ml human epidermal growth factor (Invitrogen, PHG0311), 20 ng/ml human basic fibroblast growth factor (Stemcell Technologies, 78003), 2 μg/ml heparin (Stemcell Technologies, 07980), and penicillin-streptomycin (Gibco, 15140-122). Plates were coated with 20 μg/ml laminin (Sigma, L2020 or Trevigen, 3446-005-01) for all lines except PBT-04, which were grown on uncoated plates. Cells were detached with Accutase (Sigma, A6964) for passage. Primary murine astrocytes immortalized with SV40 large T-antigen and H-RasV12 were kindly provided by Amparo Acker-Palmer (Max Planck Institute for Brain Research Frankfurt) (Depner et al., 2016). Murine astrocytes and HEK-293FT cells were maintained in D10 medium (Dulbecco's modified Eagle's medium (Gibco, 11965-092), 10% fetal bovine serum, 2 mM L-glutamine, 1 mM sodium pyruvate, 0.075% sodium bicarbonate and penicillin-streptomycin).

Antibodies

Antibody	Supplier	Catalog	Dilution
Mouse anti-N-cad (32)	BD Biosciences	610920	WB (1:1000), IF (1:200)
Rabbit anti-N-cad (H-63)	Santa Cruz	SC7939	IF (1:200)
Rabbit anti-N-cad	Proteintech	220181AP	WB (1:1000), IF (1:200)
Rabbit anti-N-cad	Cell signaling	13116	IF (1:100)
Mouse anti-p120-catenin	BD Biosciences	610133	WB (1:1000), IF (1:200)
Mouse anti-β-catenin	BD Biosciences	610153	WB (1:1000), IF (1:200)
Mouse anti-α-E-catenin	Santa Cruz	SC9988	WB (1:1000), IF (1:200)
Rabbit anti-Vimentin	Abcam	ab19348	IF (1:500)
Mouse anti-EEA1	BD Biosciences	610456	IF (1:500)
Mouse anti-Rab5	BD Biosciences	610724	IF (1:500)
Mouse anti-Rab4	BD Biosciences	610888	IF (1:500)
Mouse anti-Rab11	BD Biosciences	610656	IF (1:500)
Goat anti-LAMP1	Santa Cruz	SC8098	IF (1:500)
Mouse anti-GM130	BD Biosciences	610822	IF (1:500)
Mouse anti-YAP1	Abcam	ab56701	WB (1:500), IF (1:200)
Mouse anti-TAZ	BD Biosciences	560235	WB (1:250)
Mouse anti-Vinculin	Sigma	V9131	WB (1:10000)
Mouse anti-β-tubulin	Sigma	T7816	WB (1:10000)
Alexa-Fluor 488 donkey anti-rabbit	Invitrogen	A21206	IF (1:500)

Alexa-Fluor 568 goat anti-rabbit	Invitrogen	A11011	IF (1:500)
Alexa-Fluor 647 donkey anti-rabbit	Invitrogen	A31571	IF (1:500)
Alexa-Fluor 488 goat anti-mouse	Invitrogen	A11001	IF (1:500)
Alexa-Fluor 568 goat anti-mouse	Invitrogen	A11004	IF (1:500)
Alexa-Fluor 647 goat anti-mouse	Invitrogen	A28181	IF (1:500)
Alexa-Fluor 568 donkey anti-goat	Invitrogen	A11057	IF (1:500)
IRDye 680RD goat anti-mouse	LI-COR	926-68070	WB (1:5000)
IRDye 800CW goat anti-rabbit	LI-COR	926-32211	WB (1:5000)

DNA constructs and lentiviral transduction

Lentiviral pLKO.1-puromycin negative control and human *CDH2, CTNND1, CTNNB1* and *CTNNA1* shRNA vectors were from Sigma-Aldrich.

MISSION shRNAs	Catalog / Clone ID	Target sequences
pLKO.1-puro non-target shRNA	SHC016	GCGCGATAGCGCTAATAATTT
pLKO.1-puro *CDH2* shRNA #1	TRCN0000312701	GTGCAACAGTATACGTTAATA
pLKO.1-puro *CDH2* shRNA #2	TRCN0000053978	CCAGTGACTATTAAGAGAAAT
pLKO.1-puro *CTNND1* shRNA	TRCN0000344830	ACTACCCTCCTGATGGTTATA
pLKO.1-puro *CTNNB1* shRNA	TRCN0000314921	TCTAACCTCACTTGCAATAAT
pLKO.1-puro *CTNNA1* shRNA	TRCN0000234534	CCCTCTGTCCTCAGGTTATTA

pLenti.CAG.H2B.Dendra2.W was a gift from Rusty Lansford (Addgene plasmid #51005; RRID:Addgene_51005). N-cad WT or W161A mutated DNA were amplified by PCR from pCAG-Ncad WT or W161A-HA (Kon et al., 2019) and cloned into lentiviral pLenti-CAG-mCherry vector using NEBuilder HiFi DNA assembly (New England Biolabs, E2621) to generate pLenti-Ncad WT-HA-mCherry or pLenti-Ncad W161A-HA-mCherry.

To harvest lentiviral particles, lentiviral vector DNA was transfected with psPAX2 and pMD2.G packaging plasmids into HEK-293FT cells using Lipofectamine 2000 transfection reagent (Invitrogen, 11668019) and D10 media lacking antibiotics. After 24 hr, media were changed to glioma growth medium and virus collected for a further 40 hr. Culture media were collected and filtered through a 0.45 μM syringe filter. Glioma cells in a 6-well plate were incubated with 500 μl of viral supernatant and 500 μl growth media for at least 48 hr before selection. pLKO.1-shRNA-puromycin transduced cells were selected with 0.5 μM puromycin for 48 hr. Cells expressing H2B-Dendra2, Ncad WT-HA-mCherry or Ncad W161A-HA-mCherry constructs were sorted on a SONY MA900 Multi-Application Cell Sorter.

Electroporation

For siRNA electroporation, 1X10^6 cells were mixed with 5 μl of 20 μM siRNAs (GeneSolution siRNA, Qiagen) and 100 μl of Ingenio electroporation solution (Mirus, MIR50114) and nucleofected with an Amaxa Nucleofector I (Lonza) using program C-13 for PHGGs or T-20 for astrocytes. The efficiency of downregulation was validated using Western blot.

siRNAs	Catalog	Target sequences
Negative control siRNA	1027310	AATTCTCCGAACGTGTCACGT
CDH2 siRNA	1027417	CTGAGCTCAGTTACACTTGAA
Human *YAP1* siRNA 5	1027416	CAGGTGATACTATCAACCAAA
Human *YAP1* siRNA 8		CCGGGATGTCTCAGGAATTGA
Human *YAP1* siRNA 6		CACATCGATCAGACAACAACA
Human *YAP1* siRNA 7		TTGAAGTAGTTTAGTGTTCTA
Human *TAZ (WWTR1)* siRNA 4	1027416	ACAGTAGTACCAAATGCTTTA
Human *TAZ (WWTR1)* siRNA 3		AGACATGAGATCCATCACTAA
Human *TAZ (WWTR1)* siRNA 2		CTGGCTGTAATCACTACCATT
Human *TAZ (WWTR1)* siRNA 1		CTGCGTTCTTGTGACAGATTA

Western blot

Cells were lysed in ice-cold 1X Triton-X-100 lysis buffer (1% Triton-X-100, 150 mM NaCl, 10 mM HEPES pH7.4, 2 mM EDTA and 50 mM NaF) with additional protease and phosphatase inhibitors (10 μg/ml Aprotinin, 1 mM PMSF and 1 mM sodium vanadate), and insoluble material removed at 14,000 rpm for 10 min at 4 °C. Protein concentrations were equalized using a Pierce BCA protein assay kit (Thermo Scientific, 23225), adjusted to 1X SDS sample buffer (50 mM Tris-Cl pH6.8, 2% SDS, 0.1 % bromophenol blue, 10% glycerol), and heated to 95 °C for 5 min. Equal amounts (generally 10-20 μg) of protein were separated by sodium dodecyl sulfate-polyacrylamide gel electrophoresis and transferred to a nitrocellulose membrane. The membrane was blocked in Intercept blocking buffer (LI-COR Biosciences, 927-60003) with 5% BSA for 30 min at RT. After blocking, the membrane was probed with primary antibodies overnight at 4 °C, followed by IRDye 680RD goat anti-mouse or 800CW goat anti-rabbit conjugated secondary antibodies for 1 hr at RT. Fluorescent images were detected using the Odyssey Infrared Imaging System (LI-COR Biosciences). Quantification was performed using FIJI.

Spheroid migration and invasion

Spheroids were prepared from PBT-05 and PBT-04 cells by seeding 5X10^3 cells in multiple wells of ultra-low attachment round bottom 96-well plates (Corning, 7007) for 72 hr. Spheroids were prepared similarly from PBT-22, PBT-24 and PBT-29 cells, except the cell number was $2X10^3$ and 0.192% methylcellulose (Sigma, M0512) was included in the media. For migration assays, single spheroids were transferred with 20 μl tips to wells in 48-well plates (Corning, 3548) containing various migration substrates and incubated in 200 μl of either glioma migration medium (Human NeuroCult NS-A Proliferation kit and 20 ng/ml bFGF) or basal medium (Human NeuroCult NS-A Basal and 20 ng/ml bFGF). Phase-contrast or fluorescence images were taken at various times. The areas occupied by the spheroid and migrating cells were outlined and quantified in FIJI. The cumulative migration distance for each spheroid is the average distance between the migration front and the spheroid edge, calculated using the formula:

$$\text{Cumulative migration distance} = \sqrt{End\ migration\ area/\pi} - \sqrt{Start\ migration\ area/\pi}$$

ECM substrates To assay migration on ECM, spheroids were transferred to wells that had been coated with 20 μg/ml laminin (Sigma, L2020) or 20 μg/ml fibronectin (Sigma, F1141) overnight, drained and washed with basal media. Images were taken every 15 min for 48 hrs on an Incucyte S3 Live-cell analysis system (Sartorius, 4X/0.2). The area covered by migrating cells was measured with the Incucyte analysis program (Sartorius).

Invasion To assay invasion into Matrigel, wells were first coated with 30 μg/ml Matrigel (Corning, 356231) overnight at 4 °C and washed with basal media. Spheroids were added and allowed to attach for 1 hr at 37 °C, then covered with 100 μl 5 mg/ml Matrigel. After an additional 1 hr incubation at 37 °C, 100 μl glioma migration medium was added on top of the Matrigel-embedded spheroids. Phase-contrast images were taken every 24 hrs on Nikon Eclipse TS100. The area covered by invading cells was measured with FIJI.

Neurons To assay glioma migration on neurons, granule neuron cultures were prepared from euthanized wild-type or Rosa26$^{mT/mG}$ (expressing membrane-targeted tandem dimer Tomato) postnatal day 5 mice. Cerebella were dissected in dissection solution (1X Hank's balanced salts solution (HBSS, Gibco), 2.5 mM HEPES, 35 mM glucose, 4 mM sodium bicarbonate and 1.2 mM $MgSO_4$) and dissociated with 0.1% trypsin and 0.25 mg/ml deoxyribonuclease I (Sigma, D5319) in dissection solution for 10 min at 37 °C. After tissue fragments had settled, cells were diluted in dissection solution containing deoxyribonuclease I and centrifuged at 200Xg for 5 min. The cell pellet was suspended in granule neuron growth medium (1X Basal medium eagle (Gibco), 10% fetal bovine serum, 1 M KCl and 1X penicillin-streptomycin) and seeded in 0.1 mg/ml poly-D-lysine (Sigma, P0899) pre-coated plates for 20 min at 37 °C to deplete glia.

Unattached cells were collected and centrifuged at 200Xg for 5 min, resuspended in growth medium, and viable cells counted. $1x10^6$ cells were seeded on 0.5 mg/ml poly-D-lysine-coated sterile 12-mm diameter coverslips or aligned 700-nm diameter nanofibers in 24 well plates (Sigma, Z694533). Growth medium was changed on days in vitro (DIV) 1 and 3, adding 10 μg/ml cytosine arabinoside (AraC, Sigma, C6645) to reduce growth of non-neuronal cells. Glioma cells were seeded into 96-well ultra-low attachment round-bottom plates for spheroid production on day 2, including 2.5 μM of CytoTrace Green CMFDA (AAT Bioquest, 22017) in the media to facilitate cell tracking. On the morning and afternoon of DIV5, half of the neuron growth medium was replaced with the glioma migration medium. Glioma cell spheroids were rinsed with the NeuroCult basal medium to wash out remaining CytoTrace Green CMFDA and transferred to the neurons together with 250 μl glioma migration medium. Images were acquired every 24 hrs for 3 days on a Zeiss LSM780 confocal microscope (10X/0.45 air objective). The area covered by migrating cells on neurons was measured with FIJI.

Astrocytes To assay migration on astrocytes, we adapted the 3D astrocyte-derived scaffold procedure described previously (Gritsenko et al., 2017). $1X10^5$ immortalized murine astrocytes were cultured on 30 μg/ml Matrigel-coated 12-mm glass coverslips in D10. Astrocytes rapidly acidify glioma migration medium, so, after 2 days in D10, we added 5 mM 2-deoxy-D-glucose (Sigma, D8375) and 400 nM rotenone (Sigma, 557368) to inhibit metabolism. At day 4, glioma cell spheroids were transferred on top of astrocyte scaffolds with 500 μl glioma migration medium and cultured for a further 2 days. Cells were fixed with 4% paraformaldehyde (PFA, VWR, 100503-917), for 15 min at room temperature (RT) and stained with human-specific anti-vimentin antibodies to visualize glioma cells. Images were acquired on Leica Stellaris 5 (10X/0.40 air objective). The area covered by migrating cells was quantified with FIJI.

Astrocyte ECM Astrocytes were cultured as described above for 4 days, then lysed and the ECM washed as described previously (Harris et al., 2018). To confirm astrocyte removal, matrices were stained with anti-N-cad antibody, phalloidin and DAPI. Glioma cell spheroids were allowed to migrate for 24 hrs before staining with anti-human vimentin antibody and quantification of area covered.

N-cad ECD Fc A 96-well ELISA high-binding plate (Corning, 9018) was coated with 12.5 μg/ml recombinant human N-cad Fc chimera protein (Asp160-Ala724, R&D systems, 1388-NC) or 20 μg /ml poly-D-lysine in coating buffer (HBSS with 1 mM $CaCl_2$) overnight at 4 °C. Wells were then blocked with 3% BSA in HBSS for 2 hr at RT and washed three times in HBSS supplemented with 1.2 mM $CaCl_2$. Glioma spheroids were transferred to the pre-coated plates and incubated in glioma migration medium for 24 hr at 37 °C, 5% CO_2.

EdU incorporation

Cells were incubated with 5 μM EdU (5-ethynyl-2´-deoxyuridine) diluted in glioma growth medium for 1 hr (laminin and Matrigel) or 3 hr (neurons) at 37 °C. Cells were fixed with 4% paraformaldehyde for 15 min and permeabilized with 0.5% Triton-X-100 for 20 min at RT. EdU was detected with the Click-it 488 reaction solution (Invitrogen, C10337) for 30 min. Nuclei were stained with Hoechst 33342 for additional 30 min.

Cell tracking

Cell movements were tracked using histone H2B-Dendra2 PBT-05 cells. Spheroids were transferred to laminin or neurons for 6 hr or 24 hr respectively, before starting imaging at 15-min intervals using an Andor Dragonfly spinning disk confocal microscope (Oxford instruments, 10X/0.45 air objective). and a humidity, CO2 (5%) and temperature (37 °C) controlled chamber. The nuclear movement was tracked using Imaris (Oxford Instruments), and the directionality and velocity of individual cells were quantified using a custom-made open-source computer program, DiPer (ref. 76.)

Immunofluorescence

Cells were grown or allowed to migrate on 12-mm diameter coverglasses precoated with an appropriate substrate. Cells were fixed with 4% PFA for 15 min at RT, permeabilized with 0.1% Triton-X-100 in PBS for 10 min at RT, and blocked with 5% normal goat serum (Jackson Immunoresearch, 005-000-121), 2% BSA in PBS for 1 hr at RT. Primary antibodies were diluted in 1% BSA in PBS and incubated overnight at 4 °C. Alexa Fluor-conjugated goat anti-mouse or donkey anti-rabbit IgG (H+L) secondary antibodies were incubated together with Alexa Fluor-conjugated phalloidin (Invitrogen, A12380 or A22287) for 1 hr at RT. After 4',6-diamidino-2-phenylindole (DAPI, 1:5000) incubation for 5 min at RT, the coverglass was mounted with ProLong Glass Antifade Mount (Invitrogen, P36984). Confocal imaging was performed on a Zeiss LSM780 or a Leica Stellaris 5 confocal microscope (63X/1.40 oil objective).

N-cad antibody internalization and recycling

Glioma cell spheroids were allowed to migrate on laminin-coated coverslips for 24 hr. Coverslips were transferred to 4 °C and incubated in glioma migration medium containing 10 μg/ml rabbit anti-N-cad antibody (Proteintech, 22018-1-AP), which recognizes the N-cad extracellular domain. After 30 min, cells were washed three times with Human Neurocult NS-A basal medium and then fed with glioma migration medium. Cells were incubated for 0, 10, 20, 40 or 60 min at 37 °C and fixed with 4% PFA for 15 min at RT. For recycling, cells were allowed to internalize antibody for 40 min at 37 °C, cooled to 4 °C, and remaining cell surface antibody blocked by incubation with 0.13 mg/ml F(ab')$_2$ fragment goat-anti rabbit IgG (Jackson Immunoresearch, 111-006-045) for 30 min. The cells were then washed and incubated an additional 20 min at 37 °C to allow recycling of internalized antibody before fixation. To differentially detect surface and internalized antibody we adopted a procedure described in Carrodus et al. (Carrodus et al., 2014). Fixed cells were blocked with 5% BSA in PBS for 30 min at RT and incubated with donkey-anti-rabbit IgG (H+L) Alexa Fluor 647 (1:200), to label the cell-surface bound N-cad antibodies. After 2 hr, remaining rabbit IgG on the surface was blocked with a solution of 0.13 mg/ml AffiniPure Fab fragment goat-anti-rabbit IgG (H+L), 5% BSA in PBS, overnight at 4 °C. After blocking, cells were re-fixed with 4% PFA for 5 min at RT, then permeabilized and blocked with 0.1% Triton-X-100, 5% BSA in PBS for 30 min at RT. Another secondary antibody, donkey-anti-rabbit IgG (H+L) Alexa Fluor 488 (1:200), was used to label internalized N-cad antibodies. Additional antibodies were included at this stage to analyze N-cad colocalization with markers of specific subcellular compartments. Confocal images were acquired on Zeiss LSM780 or Leica Stellaris 5 (63X/1.40 oil objective).

The number of cell surface or intracellular N-cad antibodies-positive puncta were measured using Imaris. The Surface creation tool was used to automatically detect endosomal vesicles. The estimated XY diameter for surface detection was 0.5 μm. Background was subtracted. Colocalization of intracellular N-cad antibodies with other proteins was measured by overlapping volume between 3D surfaces of two proteins. Integrated intensities were measured using FIJI.

Transferrin uptake

Unlabeled transferrin was removed by preincubating cells in Human NeuroCult NS-A basal medium for 30 min at 37 °C. Cells were then cooled and incubated with 100 μg/ml Alexa Fluor 568-conjugated transferrin (Sigma, T23365) for 30 min at 4 °C. Cells were washed three times with the basal medium and incubated for 40 min at 37 °C before fixation and imaging.

Photoconversion

To isolate leader and follower cells for quantification of N-cad surface levels or RNA isolation, histone H2B-Dendra2 PBT-05 cell spheroids were formed for 3 days and transferred to laminin. After 24 hr, migrating leader and follower cells from 80-90 spheroids were selectively photoconverted for 5000 or 1000 ms using the 405 nm laser (FRAPPA photobleaching module, Andor iQ3 Mosaic) on an Andor Dragonfly spinning disk confocal microscope equipped with Mosaic and a humidity, CO_2 (5%) and temperature (37 °C)-controlled chamber.

To monitor switching of leader and follower cells during migration, histone H2B-Dendra2 PBT-05 cell spheroids were placed on laminin or neurons or embedded in Matrigel and allowed to migrate for 6 hr, 24 hr or 48 hr respectively. Leader cells were then photoconverted for 5000 ms as above. Images were taken after an additional 16 hr, 16 hr or 48 hr respectively, and the number of red follower cells calculated as a percentage of total red cells.

N-cad surface quantification by flow cytometry

To quantify surface N-cad by flow cytometry, cells were detached with 2 mM EDTA in HBSS for 10 min, resuspended in HBSS containing 0.5% BSA and incubated for 30 min at 4 °C with 10 µg/ml anti-N-cad primary antibody (Proteintech, 22018-1-AP). Cells were washed twice in HBSS/0.5% BSA and incubated with Alexa Fluor 647-conjugated donkey anti-rabbit IgG (H+L) secondary antibodies (1:200) for 30 min at 4 °C. Cells were analyzed by flow cytometry (BD FACSymphony A5, BD Bioscience). Data were analyzed with FlowJo (v10.9.0).

RNA sequencing

To compare RNA transcriptomes from bulk cell populations, control or N-cad shRNA cells were dissociated using Accutase at room temperature for 10 min and resuspended in HBSS. 500 cells were collected in the center of a 1.5 ml centrifuge tube containing 4.75 µl SMART-seq reaction buffer (Takara) using a BD FACSymphony S6 (BD Bioscience), avoiding cell loss on the tube walls. To compare RNA transcriptomes from leader and follower cells, approximately 90 spheroids of PBT-05 cells expressing histone H2B-Dendra2 cells were allowed to migrate for 24 hrs on laminin and photoconverted as above. After photoconversion, cells were dissociated with Accutase at room temperature, resuspended in HBSS, transferred to ice, and approximately 200 leader and follower cells were sorted into SMART-seq reaction buffer as above. Each experiment was performed on four different occasions.

RNA was prepared and cDNA was synthesized with the SMART-Seq v4 Ultra Low Input RNA Kit for Sequencing (Takara) and ran the Agilent Tapestation to assess cDNA product. To construct RNA sequencing libraries, we used Illumina's Nextera XT kit to fragment the cDNA and add barcoded sequencing adapters. Differential gene expression analysis was performed with the DEseq2 for paired sample R package (Love et al., 2014). Genes with a Benjamini-Hochberg adjusted *p*-value < 0.05 were defined as differentially expressed.

Micropattern adhesion

A micropatterned glass coverslip with disc diameters from 10 μm to 100 μm (4dcell.com) was precoated with 20 μg/ml laminin overnight at 37 °C. $1X10^5$ cells were resuspended in 1 ml of glioma migration medium and plated on the laminin-coated micropatterned glass coverslip for 1 hr at 37 °C. Unattached cells were carefully removed and fresh glioma migration medium added. After 48 hrs, cells were fixed and stained with YAP1 and N-cad antibodies. For N-cad antibody internalization, cells were allowed to internalize N-cad ECD antibodies for 40 min at 37 °C before fixation and staining as described above. The number of puncta were divided by the number of nuclei in each cluster to calculate N-cad antibody internalization per cell.

Statistics

The number of replicates for each experiment is described in the Figure legends. All experiments were repeated at least three independent biological replicates otherwise noted in the Figure legend. Statical analyses were performed using GraphPad Prism 9 and 10. *P* values were determined using Unpaired *t*-test, Paired *t*-test, Ordinary one-way ANOVA Holm-Šídák's, Šídák's, Tukey's multiple and Dunnett's multiple comparisons test and Two-way ANOVA Šídák's multiple comparisons test and Uncorrected Fisher's LSD test.

Graphics

Diagrams were prepared with Biorender.com.

Online supplemental material

Figure S1 (related to Fig. 1) N-cad expression, depletion, and controls for PHGG migration assays.

Figure S2 (related to Fig. 3 and 4) Role of intercellular N-cad homotypic interactions and importance of N-cad for catenin localization.

Figure S3 (related to Fig. 5) N-cad endocytosis, recycling and surface levels in leader and follower cells.

Figure S4 (related to Fig. 6) YAP1 signaling and wound healing gene expression is increased in leader cells.

Figure S5 (related to Fig. 8) YAP1/TAZ regulates PHGG migration and N-cad endocytosis.

Table S1 (related to Fig. 1) mRNA expression levels of cell adhesion receptors in patient-derived PHGGs.

Table S2 (related to Fig. 1) RNA sequencing results comparing control and N-cad shRNA cells.

Table S3 (related to Fig. 6) RNA sequencing results comparing leader and follower cells.

Video 1 (related to Fig. 1) Control and N-cad shRNA spheroid migration on laminin.

Video 2 (related to Fig. 6) Migrating leader and follower cells on neurons or laminin.

Acknowledgments

We are very grateful to Emily J Girard, Fiona Pakiam and Shelli Morris at Seattle Children's Research Institute for their assistance in providing cells, reagents and technical guidance during this study. We also thank Lena Schroeder, Jin Meng, Peng Guo and Julien Dubrulle in the Cellular Imaging and Bioinformatics Shared Resources at Fred Hutchinson Cancer Center for imaging and analysis assistance, Flow Cytometry core staff for cell sorting instruction, Genomics core staff at Beneroya Research Institute for sequencing and Luna Yu for computational assistance. We thank Saurav Kumar, Amanda Stainer, Liesje Steenkiste, Laura Arguedas-Jimenez, Chris Simpkins, Jay Sarthy, Mark Headley, David Helfman, Soo Young Kim and other colleagues for discussions and comments for the manuscript. This research was supported by the Fred Hutch Interdisciplinary training in Cancer Research Program, institutional funds from Fred Hutch and the shared resources of the Fred Hutch/ University of Washington Cancer Consortium (P30 CA015704).

Author contributions

Conceptualization, Methodology, Investigation, Writing – Original Draft, Visualization and Funding acquisition, D.K. and J.A.C.; Resources, J.M.O. and J.A.C.; Supervision, J.M.O. and J.A.C.

Declaration of interests

The authors declare no competing interests.

References

Akhtar, N., and N.A. Hotchin. 2001. RAC1 regulates adherens junctions through endocytosis of E-cadherin. *Mol Biol Cell*. 12:847-862.

Alieva, M., V. Leidgens, M.J. Riemenschneider, C.A. Klein, P. Hau, and J. van Rheenen. 2019. Intravital imaging of glioma border morphology reveals distinctive cellular dynamics and contribution to tumor cell invasion. *Sci Rep*. 9:2054.

Azzarelli, R., B.D. Simons, and A. Philpott. 2018. The developmental origin of brain tumours: a cellular and molecular framework. *Development*. 145.

Beadle, C., M.C. Assanah, P. Monzo, R. Vallee, S.S. Rosenfeld, and P. Canoll. 2008. The role of myosin II in glioma invasion of the brain. *Mol Biol Cell*. 19:3357-3368.

Bentley, K., C.A. Franco, A. Philippides, R. Blanco, M. Dierkes, V. Gebala, F. Stanchi, M. Jones, I.M. Aspalter, G. Cagna, S. Westrom, L. Claesson-Welsh, D. Vestweber, and H. Gerhardt. 2014. The role of differential VE-cadherin dynamics in cell rearrangement during angiogenesis. *Nat Cell Biol*. 16:309-321.

Brabetz, S., S.E.S. Leary, S.N. Grobner, M.W. Nakamoto, H. Seker-Cin, E.J. Girard, B. Cole, A.D. Strand, K.L. Bloom, V. Hovestadt, N.L. Mack, F. Pakiam, B. Schwalm, A. Korshunov, G.P. Balasubramanian, P.A. Northcott, K.D. Pedro, J. Dey, S. Hansen, S. Ditzler, P. Lichter, L. Chavez, D.T.W. Jones, J. Koster, S.M. Pfister, M. Kool, and J.M. Olson. 2018. A biobank of patient-derived pediatric brain tumor models. *Nat Med*. 24:1752-1761.

Buck, S.B., J. Bradford, K.R. Gee, B.J. Agnew, S.T. Clarke, and A. Salic. 2008. Detection of S-phase cell cycle progression using 5-ethynyl-2'-deoxyuridine incorporation with click chemistry, an alternative to using 5-bromo-2'-deoxyuridine antibodies. *Biotechniques*. 44:927-929.

Cai, D., S.C. Chen, M. Prasad, L. He, X. Wang, V. Choesmel-Cadamuro, J.K. Sawyer, G. Danuser, and D.J. Montell. 2014. Mechanical feedback through E-cadherin promotes direction sensing during collective cell migration. *Cell*. 157:1146-1159.

Camand, E., F. Peglion, N. Osmani, M. Sanson, and S. Etienne-Manneville. 2012. N-cadherin expression level modulates integrin-mediated polarity and strongly impacts on the speed and directionality of glial cell migration. *J Cell Sci*. 125:844-857.

Carrodus, N.L., K.S. Teng, K.M. Munro, M.J. Kennedy, and J.M. Gunnersen. 2014. Differential labeling of cell-surface and internalized proteins after antibody feeding of live cultured neurons. *J Vis Exp*:e51139.

Collins, C., and W.J. Nelson. 2015. Running with neighbors: coordinating cell migration and cell-cell adhesion. *Curr Opin Cell Biol*. 36:62-70.

Cuddapah, V.A., S. Robel, S. Watkins, and H. Sontheimer. 2014. A neurocentric perspective on glioma invasion. *Nat Rev Neurosci*. 15:455-465.

Davis, M.A., R.C. Ireton, and A.B. Reynolds. 2003. A core function for p120-catenin in cadherin turnover. *J Cell Biol*. 163:525-534.

Depner, C., H. Zum Buttel, N. Bogurcu, A.M. Cuesta, M.R. Aburto, S. Seidel, F. Finkelmeier, F. Foss, J. Hofmann, K. Kaulich, S. Barbus, M. Segarra, G. Reifenberger, B.K. Garvalov, T. Acker, and A. Acker-Palmer. 2016. EphrinB2 repression through ZEB2 mediates tumour invasion and anti-angiogenic resistance. *Nat Commun*. 7:12329.

Friedl, P., and R. Mayor. 2017. Tuning Collective Cell Migration by Cell-Cell Junction Regulation. *Cold Spring Harb Perspect Biol*. 9.

Ganzler-Odenthal, S.I., and C. Redies. 1998. Blocking N-cadherin function disrupts the epithelial structure of differentiating neural tissue in the embryonic chicken brain. *J Neurosci*. 18:5415-5425.

Gravendeel, L.A., M.C. Kouwenhoven, O. Gevaert, J.J. de Rooi, A.P. Stubbs, J.E. Duijm, A. Daemen, F.E. Bleeker, L.B. Bralten, N.K. Kloosterhof, B. De Moor, P.H. Eilers, P.J. van der Spek, J.M. Kros, P.A. Sillevis Smitt, M.J. van den Bent, and P.J. French. 2009. Intrinsic gene expression profiles of gliomas are a better predictor of survival than histology. *Cancer Res*. 69:9065-9072.

Gritsenko, P., W. Leenders, and P. Friedl. 2017. Recapitulating in vivo-like plasticity of glioma cell invasion along blood vessels and in astrocyte-rich stroma. *Histochem Cell Biol*. 148:395-406.

Gritsenko, P.G., N. Atlasy, C.E.J. Dieteren, A.C. Navis, J.H. Venhuizen, C. Veelken, D. Schubert, A. Acker-Palmer, B.A. Westerman, T. Wurdinger, W. Leenders, P. Wesseling, H.G. Stunnenberg, and P. Friedl. 2020. p120-catenin-dependent collective brain infiltration by glioma cell networks. *Nat Cell Biol*. 22:97-107.

Gritsenko, P.G., and P. Friedl. 2018. Adaptive adhesion systems mediate glioma cell invasion in complex environments. *J Cell Sci*. 131.

Gritsenko, P.G., O. Ilina, and P. Friedl. 2012. Interstitial guidance of cancer invasion. *J Pathol*. 226:185-199.

Harris, G.M., I. Raitman, and J.E. Schwarzbauer. 2018. Cell-derived decellularized extracellular matrices. *Methods Cell Biol*. 143:97-114.

Harris, T.J., and M. Peifer. 2005. Decisions, decisions: beta-catenin chooses between adhesion and transcription. *Trends Cell Biol*. 15:234-237.

Harris, T.J., and U. Tepass. 2010. Adherens junctions: from molecules to morphogenesis. *Nat Rev Mol Cell Biol*. 11:502-514.

Hatta, K., and M. Takeichi. 1986. Expression of N-cadherin adhesion molecules associated with early morphogenetic events in chick development. *Nature*. 320:447-449.

Jakobsson, L., C.A. Franco, K. Bentley, R.T. Collins, B. Ponsioen, I.M. Aspalter, I. Rosewell, M. Busse, G. Thurston, A. Medvinsky, S. Schulte-Merker, and H. Gerhardt. 2010. Endothelial cells dynamically compete for the tip cell position during angiogenic sprouting. *Nat Cell Biol*. 12:943-953.

Jones, C., L. Perryman, and D. Hargrave. 2012. Paediatric and adult malignant glioma: close relatives or distant cousins? *Nat Rev Clin Oncol*. 9:400-413.

Jossin, Y., and J.A. Cooper. 2011. Reelin, Rap1 and N-cadherin orient the migration of multipolar neurons in the developing neocortex. *Nat Neurosci*. 14:697-703.

Julich, D., G. Cobb, A.M. Melo, P. McMillen, A.K. Lawton, S.G. Mochrie, E. Rhoades, and S.A. Holley. 2015. Cross-Scale Integrin Regulation Organizes ECM and Tissue Topology. *Dev Cell*. 34:33-44.

Kadowaki, M., S. Nakamura, O. Machon, S. Krauss, G.L. Radice, and M. Takeichi. 2007. N-cadherin mediates cortical organization in the mouse brain. *Dev Biol*. 304:22-33.

Katsuno-Kambe, H., and A.S. Yap. 2020. Endocytosis, cadherins and tissue dynamics. *Traffic*. 21:268-273.

Kawauchi, T., K. Sekine, M. Shikanai, K. Chihama, K. Tomita, K. Kubo, K. Nakajima, Y. Nabeshima, and M. Hoshino. 2010. Rab GTPases-dependent endocytic pathways regulate neuronal migration and maturation through N-cadherin trafficking. *Neuron*. 67:588-602.

Khalil, A.A., and J. de Rooij. 2019. Cadherin mechanotransduction in leader-follower cell specification during collective migration. *Exp Cell Res*. 376:86-91.

Kim, J., Y.H. Kim, J. Kim, D.Y. Park, H. Bae, D.H. Lee, K.H. Kim, S.P. Hong, S.P. Jang, Y. Kubota, Y.G. Kwon, D.S. Lim, and G.Y. Koh. 2017. YAP/TAZ regulates sprouting angiogenesis and vascular barrier maturation. *J Clin Invest*. 127:3441-3461.

Kim, N.G., E. Koh, X. Chen, and B.M. Gumbiner. 2011. E-cadherin mediates contact inhibition of proliferation through Hippo signaling-pathway components. *Proc Natl Acad Sci U S A*. 108:11930-11935.

Kluiver, T.A., M. Alieva, D.G. van Vuurden, E.J. Wehrens, and A.C. Rios. 2020. Invaders Exposed: Understanding and Targeting Tumor Cell Invasion in Diffuse Intrinsic Pontine Glioma. *Front Oncol*. 10:92.

Kon, E., E. Calvo-Jimenez, A. Cossard, Y. Na, J.A. Cooper, and Y. Jossin. 2019. N-cadherin-regulated FGFR ubiquitination and degradation control mammalian neocortical projection neuron migration. *Elife*. 8.

Konen, J., E. Summerbell, B. Dwivedi, K. Galior, Y. Hou, L. Rusnak, A. Chen, J. Saltz, W. Zhou, L.H. Boise, P. Vertino, L. Cooper, K. Salaita, J. Kowalski, and A.I. Marcus. 2017. Image-guided genomics of phenotypically heterogeneous populations reveals vascular signalling during symbiotic collective cancer invasion. *Nat Commun*. 8:15078.

Kuriyama, S., E. Theveneau, A. Benedetto, M. Parsons, M. Tanaka, G. Charras, A. Kabla, and R. Mayor. 2014. In vivo collective cell migration requires an LPAR2-dependent increase in tissue fluidity. *J Cell Biol*. 206:113-127.

Le, T.L., A.S. Yap, and J.L. Stow. 1999. Recycling of E-cadherin: a potential mechanism for regulating cadherin dynamics. *J Cell Biol*. 146:219-232.

Love, M.I., W. Huber, and S. Anders. 2014. Moderated estimation of fold change and dispersion for RNA-seq data with DESeq2. *Genome Biol*. 15:550.

Mui, K.L., C.S. Chen, and R.K. Assoian. 2016. The mechanical regulation of integrin-cadherin crosstalk organizes cells, signaling and forces. *J Cell Sci*. 129:1093-1100.

Nanes, B.A., C. Chiasson-MacKenzie, A.M. Lowery, N. Ishiyama, V. Faundez, M. Ikura, P.A. Vincent, and A.P. Kowalczyk. 2012. p120-catenin binding masks an endocytic signal conserved in classical cadherins. *J Cell Biol*. 199:365-380.

Neto, F., A. Klaus-Bergmann, Y.T. Ong, S. Alt, A.C. Vion, A. Szymborska, J.R. Carvalho, I. Hollfinger, E. Bartels-Klein, C.A. Franco, M. Potente, and H. Gerhardt. 2018. YAP and TAZ regulate adherens junction dynamics and endothelial cell distribution during vascular development. *Elife*. 7.

Neve, A., K. Santhana Kumar, D. Tripolitsioti, M.A. Grotzer, and M. Baumgartner. 2017. Investigation of brain tissue infiltration by medulloblastoma cells in an ex vivo model. *Sci Rep*. 7:5297.

Ng, M.R., A. Besser, G. Danuser, and J.S. Brugge. 2012. Substrate stiffness regulates cadherin-dependent collective migration through myosin-II contractility. *J Cell Biol*. 199:545-563.

Nguyen, T., L. Duchesne, G.H.N. Sankara Narayana, N. Boggetto, D.D. Fernig, C. Uttamrao Murade, B. Ladoux, and R.M. Mege. 2019. Enhanced cell-cell contact stability and decreased N-cadherin-mediated migration upon fibroblast growth factor receptor-N-cadherin cross talk. *Oncogene*. 38:6283-6300.

Noh, M.G., S.J. Oh, E.J. Ahn, Y.J. Kim, T.Y. Jung, S. Jung, K.K. Kim, J.H. Lee, K.H. Lee, and K.S. Moon. 2017. Prognostic significance of E-cadherin and N-cadherin expression in Gliomas. *BMC Cancer*. 17:583.

Orr, B.A., H. Bai, Y. Odia, D. Jain, R.A. Anders, and C.G. Eberhart. 2011. Yes-associated protein 1 is widely expressed in human brain tumors and promotes glioblastoma growth. *J Neuropathol Exp Neurol*. 70:568-577.

Osswald, M., E. Jung, F. Sahm, G. Solecki, V. Venkataramani, J. Blaes, S. Weil, H. Horstmann, B. Wiestler, M. Syed, L. Huang, M. Ratliff, K. Karimian Jazi, F.T. Kurz, T. Schmenger, D. Lemke, M. Gommel, M. Pauli, Y. Liao, P. Haring, S. Pusch, V. Herl, C. Steinhauser, D. Krunic, M. Jarahian, H. Miletic, A.S. Berghoff, O. Griesbeck, G. Kalamakis, O. Garaschuk, M. Preusser, S. Weiss, H. Liu, S. Heiland, M. Platten, P.E. Huber, T. Kuner, A. von Deimling, W. Wick, and F. Winkler. 2015. Brain tumour cells interconnect to a functional and resistant network. *Nature*. 528:93-98.

Ouyang, M., S. Lu, T. Kim, C.E. Chen, J. Seong, D.E. Leckband, F. Wang, A.B. Reynolds, M.A. Schwartz, and Y. Wang. 2013. N-cadherin regulates spatially polarized signals through distinct p120ctn and beta-catenin-dependent signalling pathways. *Nat Commun*. 4:1589.

Panciera, T., L. Azzolin, M. Cordenonsi, and S. Piccolo. 2017. Mechanobiology of YAP and TAZ in physiology and disease. *Nat Rev Mol Cell Biol*. 18:758-770.

Peglion, F., F. Llense, and S. Etienne-Manneville. 2014. Adherens junction treadmilling during collective migration. *Nat Cell Biol*. 16:639-651.

Reynolds, A.B., and A. Roczniak-Ferguson. 2004. Emerging roles for p120-catenin in cell adhesion and cancer. *Oncogene*. 23:7947-7956.

Sandilands, E., E.C. Freckmann, E.M. Cumming, A. Roman-Fernandez, L. McGarry, J. Anand, L. Galbraith, S. Mason, R. Patel, C. Nixon, J. Cartwright, H.Y. Leung, K. Blyth, and D.M. Bryant. 2023. The small GTPase ARF3 controls invasion modality and metastasis by regulating N-cadherin levels. *J Cell Biol*. 222.

Saxena, K., M.K. Jolly, and K. Balamurugan. 2020. Hypoxia, partial EMT and collective migration: Emerging culprits in metastasis. *Transl Oncol*. 13:100845.

Scarpa, E., A. Szabo, A. Bibonne, E. Theveneau, M. Parsons, and R. Mayor. 2015. Cadherin Switch during EMT in Neural Crest Cells Leads to Contact Inhibition of Locomotion via Repolarization of Forces. *Dev Cell*. 34:421-434.

Shapiro, L., A.M. Fannon, P.D. Kwong, A. Thompson, M.S. Lehmann, G. Grubel, J.F. Legrand, J. Als-Nielsen, D.R. Colman, and W.A. Hendrickson. 1995. Structural basis of cell-cell adhesion by cadherins. *Nature*. 374:327-337.

Tamura, K., W.S. Shan, W.A. Hendrickson, D.R. Colman, and L. Shapiro. 1998. Structure-function analysis of cell adhesion by neural (N-) cadherin. *Neuron*. 20:1153-1163.

Te Boekhorst, V., and P. Friedl. 2016. Plasticity of Cancer Cell Invasion-Mechanisms and Implications for Therapy. *Adv Cancer Res*. 132:209-264.

Theveneau, E., L. Marchant, S. Kuriyama, M. Gull, B. Moepps, M. Parsons, and R. Mayor. 2010. Collective chemotaxis requires contact-dependent cell polarity. *Dev Cell*. 19:39-53.

Totaro, A., T. Panciera, and S. Piccolo. 2018. YAP/TAZ upstream signals and downstream responses. *Nat Cell Biol*. 20:888-899.

Vassilev, V., A. Platek, S. Hiver, H. Enomoto, and M. Takeichi. 2017. Catenins Steer Cell Migration via Stabilization of Front-Rear Polarity. *Dev Cell*. 43:463-479 e465.

Venkataramani, V., Y. Yang, M.C. Schubert, E. Reyhan, S.K. Tetzlaff, N. Wissmann, M. Botz, S.J. Soyka, C.A. Beretta, R.L. Pramatarov, L. Fankhauser, L. Garofano, A. Freudenberg, J. Wagner, D.I. Tanev, M. Ratliff, R. Xie, T. Kessler, D.C. Hoffmann, L. Hai, Y. Dorflinger, S. Hoppe, Y.A. Yabo, A. Golebiewska, S.P. Niclou, F. Sahm, A. Lasorella, M. Slowik, L. Doring, A. Iavarone, W. Wick, T. Kuner, and F. Winkler. 2022. Glioblastoma hijacks neuronal mechanisms for brain invasion. *Cell*. 185:2899-2917 e2831.

Vinci, M., A. Burford, V. Molinari, K. Kessler, S. Popov, M. Clarke, K.R. Taylor, H.N. Pemberton, C.J. Lord, A. Gutteridge, T. Forshew, D. Carvalho, L.V. Marshall, E.Y. Qin, W.J. Ingram, A.S. Moore, H.K. Ng, S. Trabelsi, D. H'Mida-Ben Brahim, N. Entz-Werle, S. Zacharoulis, S. Vaidya, H.C. Mandeville, L.R. Bridges, A.J. Martin, S. Al-Sarraj, C. Chandler, M. Sunol, J. Mora, C. de Torres, O. Cruz, A.M. Carcaboso, M. Monje, A. Mackay, and C. Jones. 2018. Functional diversity and cooperativity between subclonal populations of pediatric glioblastoma and diffuse intrinsic pontine glioma cells. *Nat Med*. 24:1204-1215.

Wint, H., J. Li, T. Abe, H. Yamada, T. Higaki, Y. Nasu, M. Watanabe, K. Takei, and T. Takeda. 2023. Pacsin 2-dependent N-cadherin internalization regulates the migration behaviour of malignant cancer cells. *J Cell Sci*. 136.

Wu, J.S., J. Jiang, B.J. Chen, K. Wang, Y.L. Tang, and X.H. Liang. 2021. Plasticity of cancer cell invasion: Patterns and mechanisms. *Transl Oncol*. 14:100899.

Xu, X., W.E. Li, G.Y. Huang, R. Meyer, T. Chen, Y. Luo, M.P. Thomas, G.L. Radice, and C.W. Lo. 2001. Modulation of mouse neural crest cell motility by N-cadherin and connexin 43 gap junctions. *J Cell Biol*. 154:217-230.

Zanconato, F., M. Cordenonsi, and S. Piccolo. 2019. YAP and TAZ: a signalling hub of the tumour microenvironment. *Nat Rev Cancer*. 19:454-464.

Zarco, N., E. Norton, A. Quinones-Hinojosa, and H. Guerrero-Cazares. 2019. Overlapping migratory mechanisms between neural progenitor cells and brain tumor stem cells. *Cell Mol Life Sci*. 76:3553-3570.

Zhang, J., K.F. Goliwas, W. Wang, P.V. Taufalele, F. Bordeleau, and C.A. Reinhart-King. 2019. Energetic regulation of coordinated leader-follower dynamics during collective invasion of breast cancer cells. *Proc Natl Acad Sci U S A*. 116:7867-7872.

Figure 1

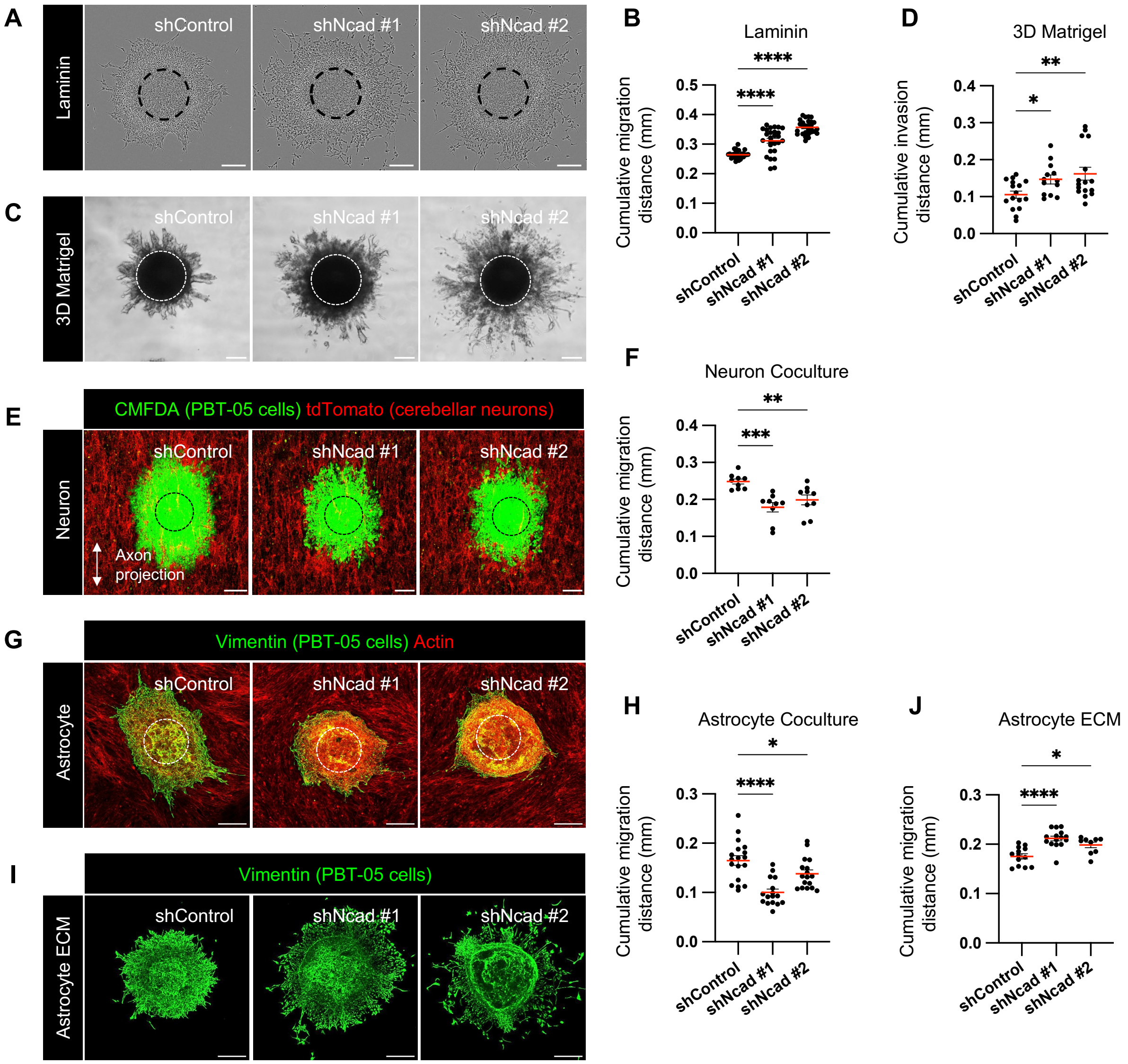

Figure 1. N-cad inhibits PHGG migration on ECM but stimulates migration on neurons and astrocytes. (A, B) Representative images and quantification of cumulative migration distance for control or N-cad shRNA PBT-05 spheroids plated on laminin for 24 hrs. (C, D) Representative images and quantification of invasion in 3D Matrigel for 96 hrs. (E, F) Images and quantification of migration on neurons for 72 hrs. PBT-05 spheroids were labeled with cell-permeable Green CMFDA fluorescent dye before transferring to tdTomato-expressing cerebellar neurons that had differentiated along aligned nanofibers. (G, H) Images and quantification of migration on mouse astrocyte cultures for 48 hrs. PBT-05 cells were detected with human-specific anti-vimentin antibodies. PBT-05 cell and astrocyte actin was detected with

phalloidin. (I, J) Images and quantification of migration on astrocyte-derived decellularized ECM for 24 hrs. (A, C, E, G, I) Dashed circles represent spheroid at 0 hrs. Scale bars, 200 μm. (B, D, F, H, J) Error bars indicate mean±s.e.m.

Ordinary one-way ANOVA Holm-Šídák's multiple comparisons tests. **P*<0.05, ***P*<0.01, ****P*<0.001, *****P*<0.0001. (B) N=27-29 spheroids, 3 experiments. (D) N=13-16 spheroids, 4 experiments. (F) N=9 spheroids, 3 experiments. (H) N=16-18 spheroids, 3 experiments. (J) N=9-15 spheroids, 2 experiments.

Figure 2

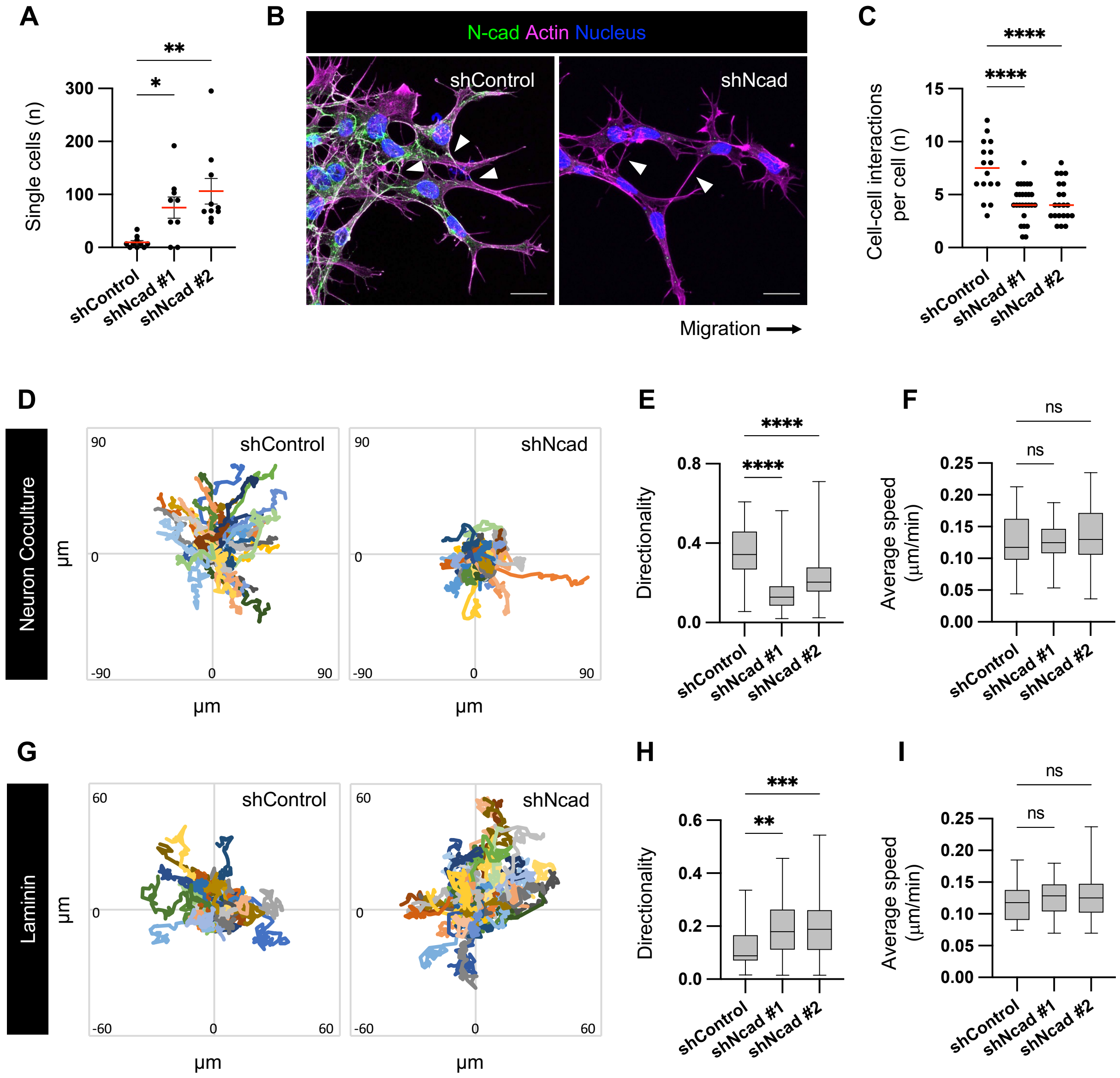

Figure 2. N-cad regulates PHGG cell cohesion during migration. (A) Number of single cells migrating ahead of the migration front after 24 hrs migration on laminin. (B) Images and (C) quantification of cell-cell connections at the migration front. Scale bar, 20 µm. Error bars show mean±s.e.m. (D-I) Cell tracking Dendra2-histone H2B-expressing control or N-cad shRNA cells migrating on neurons or laminin for 16 hrs. (D, G) cell tracks and (E, F, H, I) box and whisker plots indicating median, quartiles and range.

Ordinary one-way ANOVA Holm-Šídák's multiple comparisons tests. ns, not significant, *$P<0.05$, **$P<0.01$, ***$P<0.001$, ****$P<0.0001$. (A) N=12 spheroids. (C) N=16-26 spheroids, 3 experiments. (E-F) N=42-102 cells, 3 spheroids. (H-I) N=49-70 cells, 3 spheroids.

Figure 3

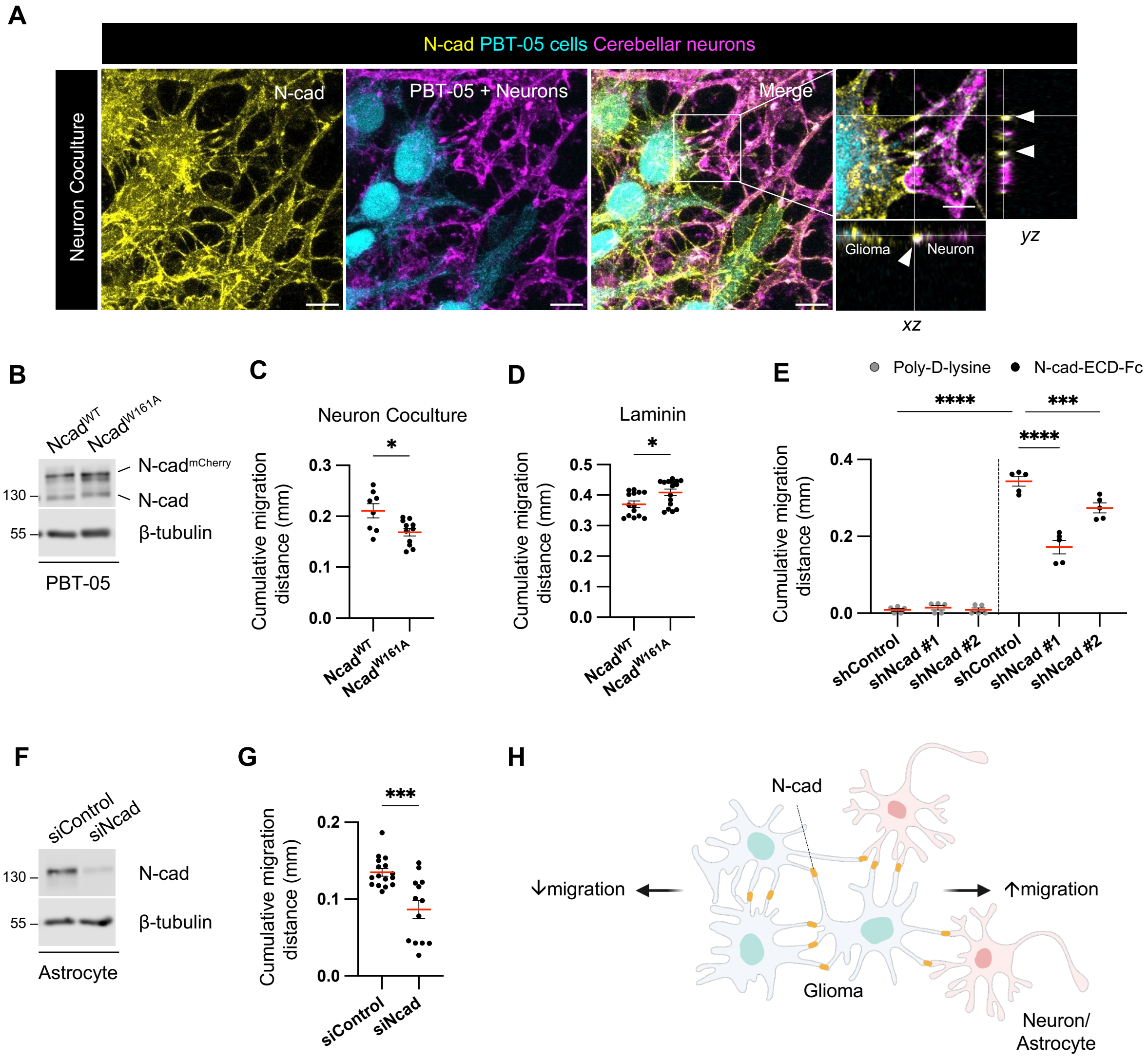

Figure 3. Intercellular N-cad homotypic interactions slow PHGG migration on ECM and speed migration on neurons and astrocytes. (A) N-cad in intercellular contacts between migrating PBT-05 cells, labeled with Green CMFDA, and cerebellar neurons expressing tdTomato. Migration for 72 hrs before fixation and staining with N-cad antibody. *xy* images are maximum intensity projections from multiple *z*-planes. Insets show enlarged *xy*, *xz* and *yz* images. Arrowheads indicate N-cad at cell-cell contacts. Scale bars, 20 μm and 5 μm (inset). (B) Western blot analysis for Ncad^{WT}-mCherry or Ncad^{W161A}-mCherry expression in PBT-05 cells. β-tubulin is shown as a loading control. (C) Cumulative migration distances on neurons for 72 hrs. Error bars show mean±s.e.m. (D) Cumulative migration distance on laminin for 24 hrs. (E) N-cad in the environment stimulates PHGG migration. Migration on poly-D-lysine or N-cad extracellular domain (ECD)-Fc surfaces for 24 hrs. (F-G) Astrocyte N-cad stimulates PHGG

migration. (F) Western blot shows N-cad siRNA depletes N-cad from mouse astrocytes. β-tubulin is shown as a loading control. (G) Cumulative migration distances on control or N-cad-depleted astrocytes for 48 hrs. (H) Model diagram: migration on ECM is slowed by N-cad-mediated glioma-glioma interactions but migration on neurons or astrocytes is accelerated by N-cad-mediated glioma binding to surrounding neural cells.

(C, D, G) Unpaired *t*-test. (E) Ordinary one-way ANOVA Šídák's multiple comparisons test. **P*<0.05, ****P*<0.001, *****P*<0.0001. (C) N=8-11 spheroids, 3 experiments. (D) N=14-16 spheroids, 3 experiments. (E) N=5 spheroids, 2 experiments. (G) N=13-16 spheroids, 3 experiments.

Figure 4

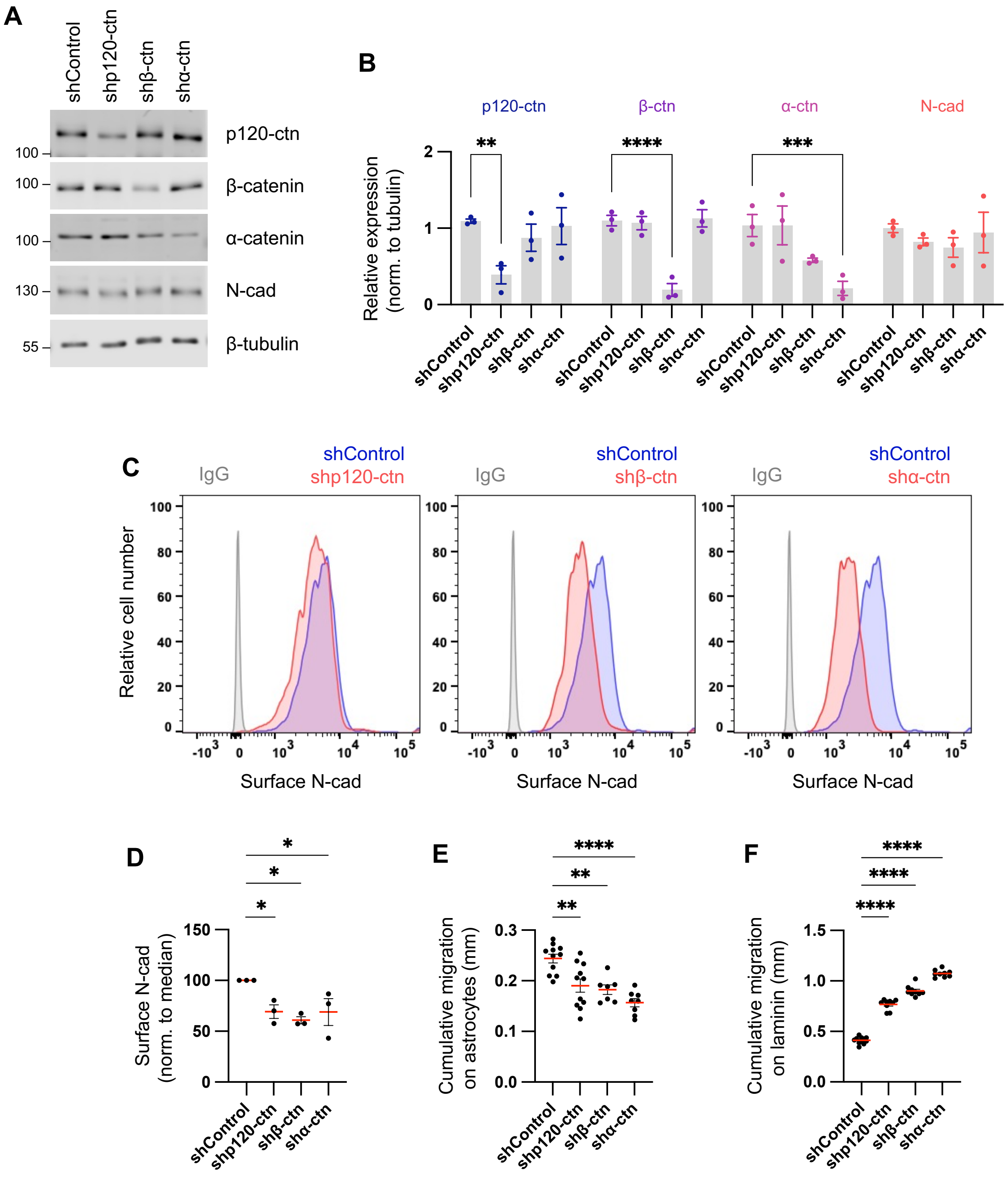

Figure 4. Catenins regulate N-cad levels and cell migration. (A-B) Western blot analysis of control, p120-catenin (p120-ctn), β-catenin (β-ctn) and α-catenin (α-ctn) in PBT-05 cells expressing various shRNAs. Protein levels were normalized to β-tubulin as a loading control. Error bars show mean±s.e.m. Two-way ANOVA Uncorrected Fisher's LSD test. N=3 Western blots. (C-D) Representative histograms and quantification of N-cad surface levels in control and catenin-depleted cells measured by flow cytometry. Ordinary one-way ANOVA with Dunnett's

multiple comparisons test. N=3 experiments. (E-F) Cumulative migration distances on (E) astrocytes for 48 hrs and (F) laminin for 24 hrs. Ordinary one-way ANOVA Dunnett's multiple comparisons test. N=7-11 spheroids, 2 experiments. *$P<0.05$, **$P<0.01$, ***$P<0.001$, ****$P<0.0001$.

Figure 5

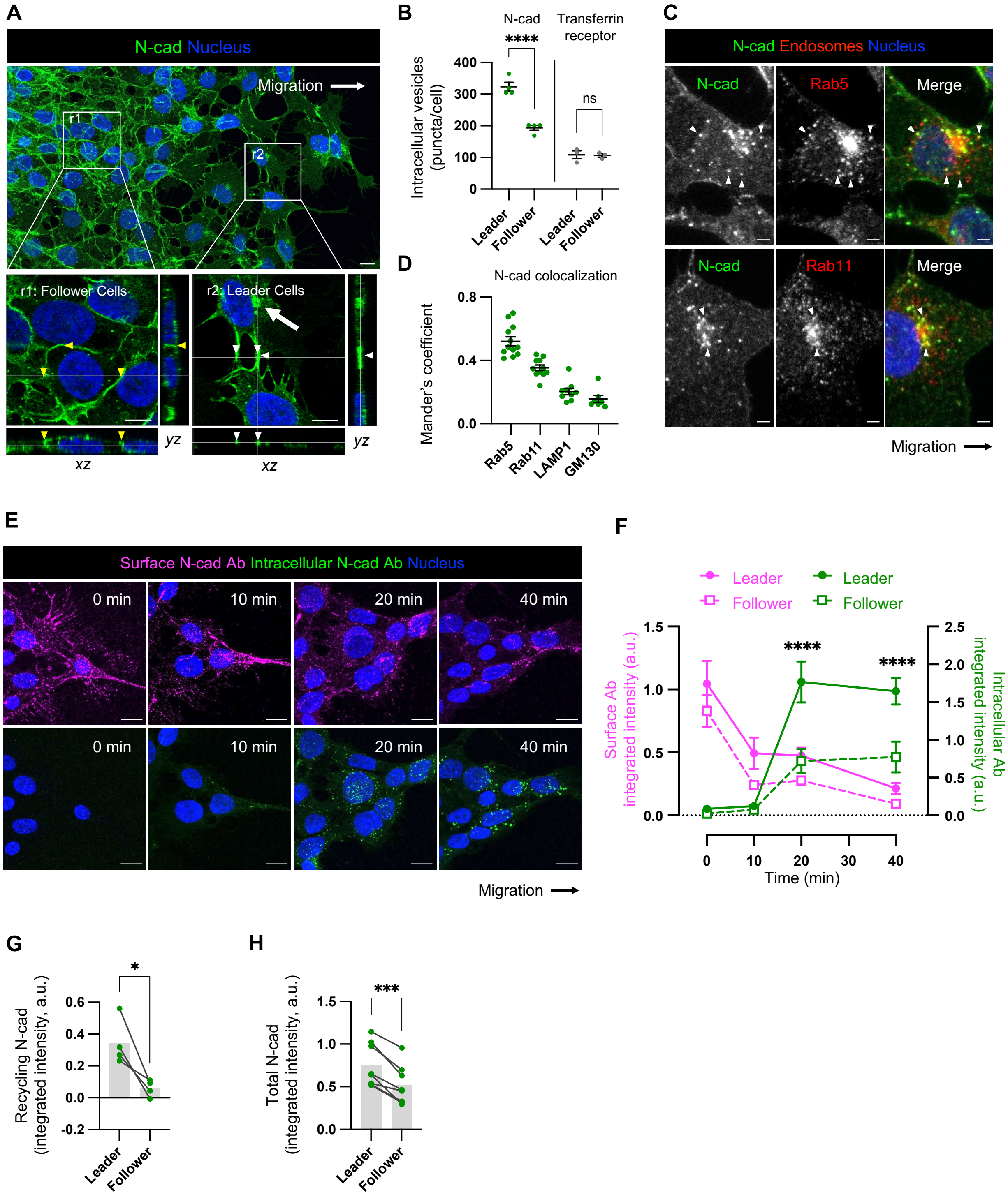

Figure 5. Distinct N-cad localization and dynamics in leader and follower cells. (A) Localization of N-cad in PBT-05 cells migrating on laminin. Maximum intensity projections. Insets show enlarged orthogonal views of follower (r1) and leader (r2) cells. Arrowheads indicate cell-cell junctions and arrows indicate vesicles. Scale bars, 10 µm or 7 µm (inset). (B)

Intracellular N-cad or transferrin receptor-positive vesicles per cell were counted in leader and follower cells. N=3 experiments. Unpaired *t*-test. ****P*<0.0001. ns, not significant. (C) Representative images showing colocalization between N-cad and endosomal markers. Arrowheads indicate N-cad-positive endocytic vesicles colocalized with Rab5 or Rab11. Scale bars, 10 μm or 2 μm (inset). (D) Mander's colocalization coefficients. N=7-12 cells, 2-3 spheroids for each marker protein analyzed. (E-F) N-cad antibody uptake assay. Surface N-cad was labeled with N-cad ECD antibodies on ice before warming for various times, fixing, and staining for surface and intracellular antibody as described in Fig. S3 A. (E) Representative images. Scale bars, 10 μm. (F) Quantification. a.u., arbitrary units. N=7-24 cells, 2-4 spheroids, 2 experiments. Two-way ANOVA Tukey's multiple comparisons test between leader and follower cells at the same time point. *****P*<0.0001. (G) Recycling of intracellular N-cad Abs to the surface in leader and follower cells, measured as described in Fig. S3 E. N=4 experiments each representing the average of 10 cells in each of 3-5 spheroids. Paired *t*-test. **P*<0.05. (H) Quantification of total N-cad fluorescence intensity in leader and follower cells. Migrating cells were fixed, permeabilized and stained with N-cad Ab. Fluorescence intensity was integrated for multiple leader and follower cells across the *z* stack. Paired *t*-test. ****P*<0.001. N=8 spheroids, 5 experiments.

Figure 6

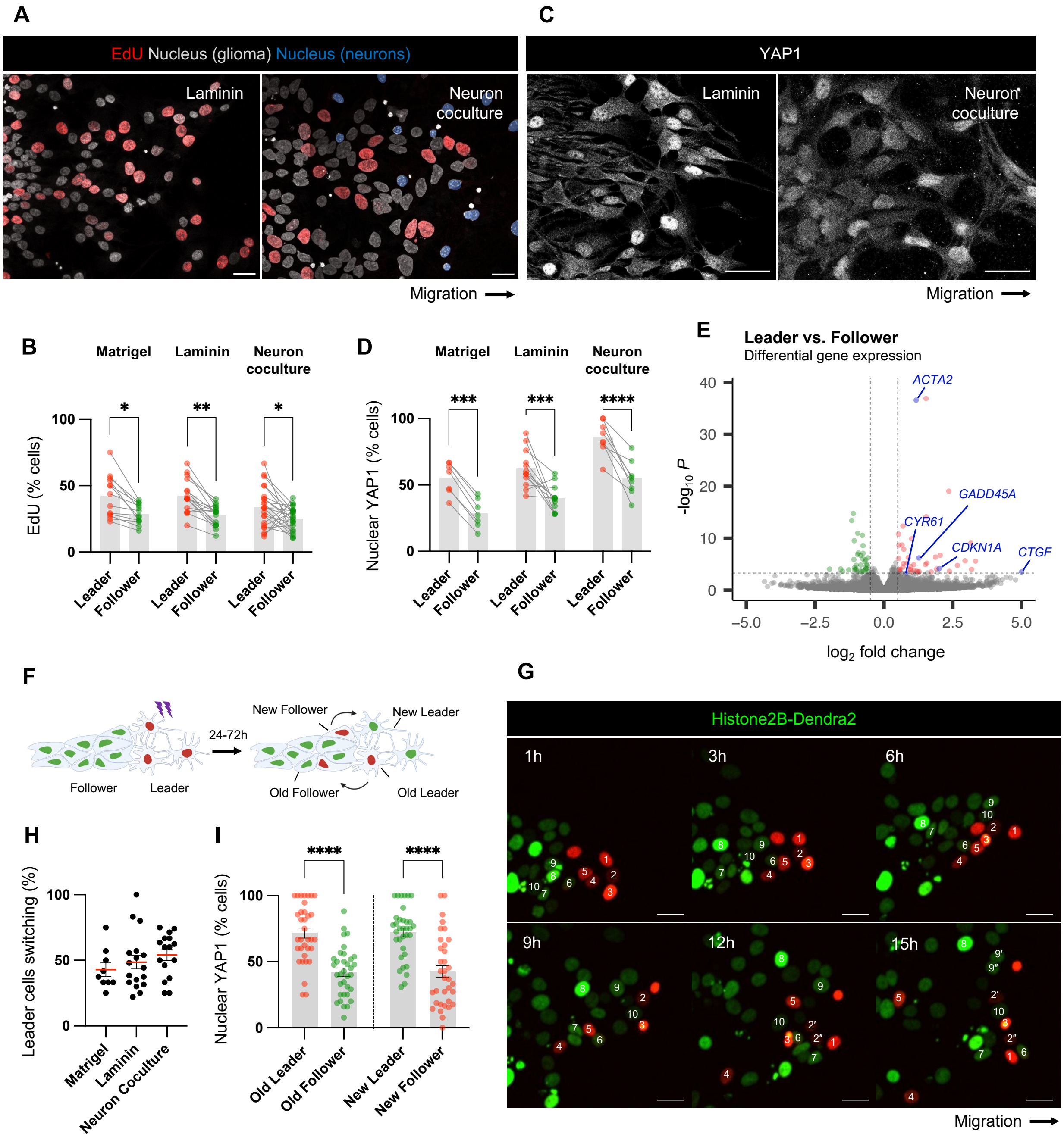

Figure 6. Increased DNA synthesis and YAP1/TAZ signaling in leader cells. (A, C) EdU or YAP1 in leader (L) and follower (F) cells in spheroid cell migration on laminin for 24 hrs or neurons for 72 hrs. Scale bars, 20 μm. (B, D) Quantification of the percentage of EdU or nuclear YAP1-positive leader and follower cells. PBT-05 spheroids invaded or migrated in Matrigel for 96 hrs, laminin for 24 hrs and neurons for 72 hrs. (B) N=13-23 spheroids, 3-4 experiments. (D) N=7-12 spheroids, 3 experiments. (E) RNA sequencing data of leader and follower cells. Each

point in the Volcano plots represents a differentially expressed gene from 4 biological replicates. Genes with at least log2 fold change > 0.5 and FDR < 0.05 were colored. Red represents up-regulated genes and green represents down-regulated genes in leader cells compared with follower cells. Blue represents the YAP1-response genes. (F) Schematic diagram of photoconversion of histone H2B-Dendra2 expressing leader cells. (G) Representative images from a time-lapse movie of histone H2B-Dendra2 spheroid migration on laminin. Scale bars, 20 μm. (H) The percentage of leader cells switching positions with follower cells in Matrigel (48 hr after photoconversion, N=9 spheroids), laminin (16 hr after photoconversion, 17 spheroids) and neurons (16 hr after photoconversion, 16 spheroids). (I) Migrating histone H2B-Dendra2 expressing PBT-05 cells were fixed and permeabilized 24 hrs after photoconversion and processed for YAP1 immunofluorescence. The percent of old and new leaders and followers with nuclear YAP1 was calculated. N=34 spheroids, 3 experiments.

(B, D) Two-way ANOVA Šídák's multiple comparisons test. (I) Ordinary one-way ANOVA Tukey's multiple comparisons test. **P*<0.05, ***P*<0.001, ****P*<0.001, *****P*<0.0001.

Figure 7

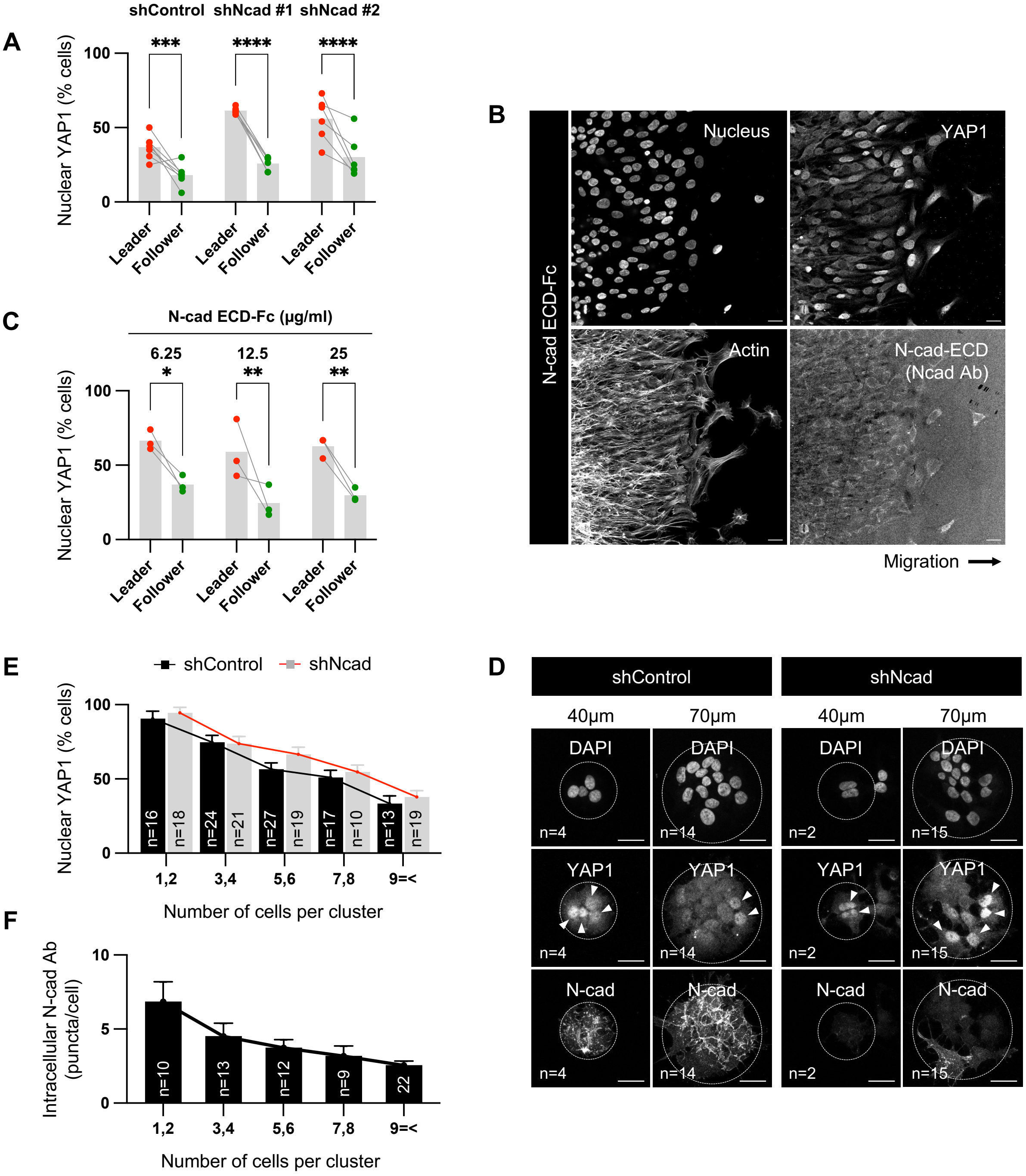

Figure 7. YAP1 regulation by cell density independent of N-cad. (A) Effect of N-cad depletion on YAP1 localization in migrating PBT-05 cells. (B-C) Effect of extracellular N-cad on YAP1 localization. Representative images of cells migrating on 12.5 μg/ml N-cad ECD-Fc coated surface for 24 hrs and quantification of percent nuclear YAP1 after migration on 6.25,

12.5 or 25 μg/ml N-cad ECD-Fc. (D) Representative images of control and N-cad shRNA cells on 40 or 70 μm laminin-coated discs for 48 hrs before fixation and staining for YAP1 and N-cad. The number of cells per cluster is noted in lower left. Arrowheads indicate cells with nuclear YAP1. Scale bar, 20 μm. (E) Quantification of percent cells with nuclear YAP1 in different size clusters of shControl and shNcad cells. (F) N-cad antibody uptake by cells in different size clusters.

(A, C) Two-way ANOVA Šídák's multiple comparisons test. **P*<0.05, ***P*<0.001, ****P*<0.001, *****P*<0.0001. (A) N=6-7 spheroids, 3 experiments. (B) N=3 spheroids in each condition. (E, F) The number of clusters quantified is noted on the graph.

Figure 8

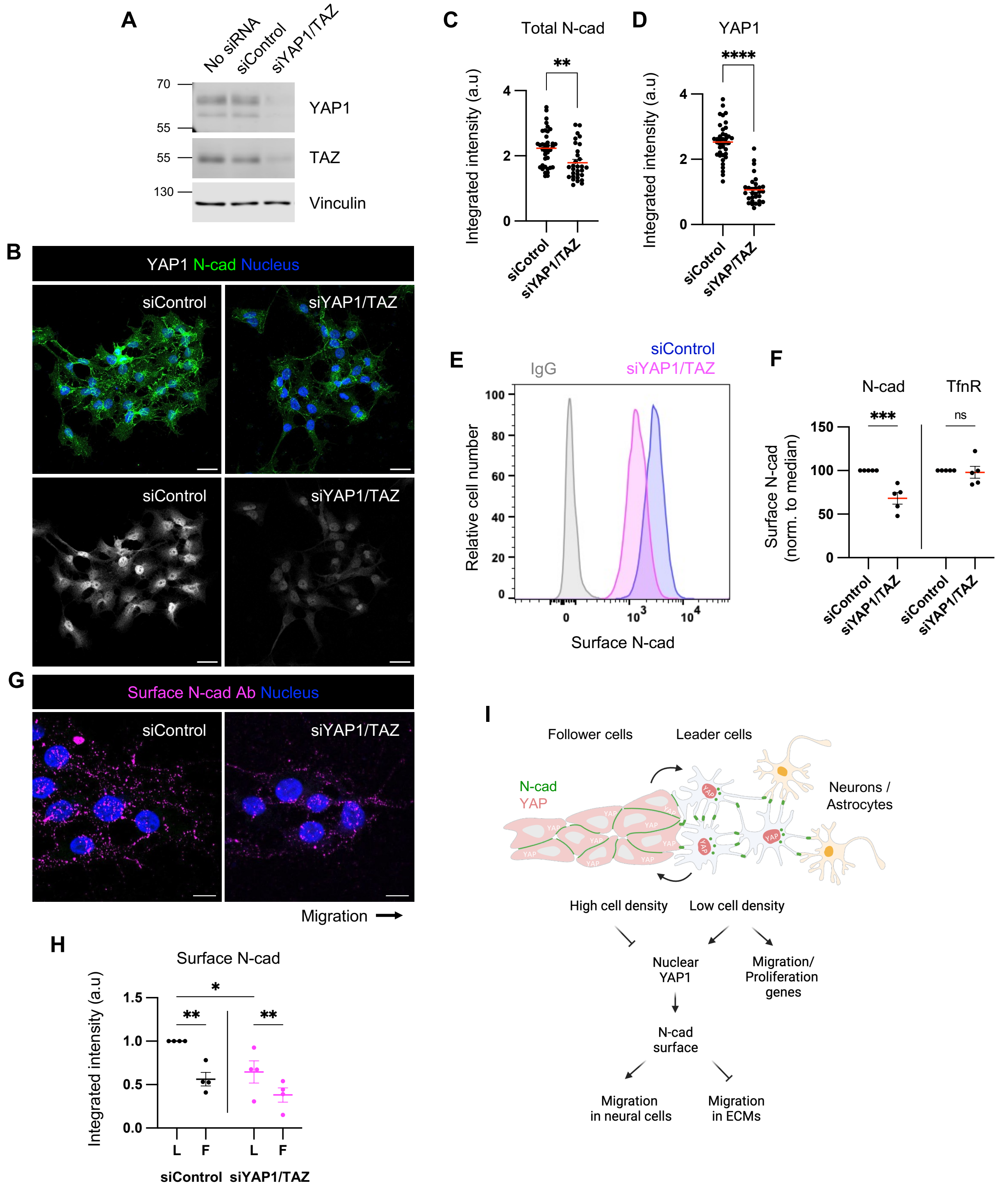

Figure 8. YAP1/TAZ regulates N-cad surface level during PHGG migration. (A) Western blot analysis of control or YAP1/TAZ siRNA-treated cells. Vinculin is shown as a loading control. (B-D) Representative images and quantification of total N-cad in low-density cultures of control

and YAP1/TAZ-depleted cells. Maximum intensity projections. Scale bars, 20 μm. a.u., arbitrary units. (E-F) Representative histograms and quantification of N-cad surface levels in low-density cultures of control and YAP1/TAZ-depleted cells measured by flow cytometry. (G-H) Representative images and quantification of surface N-cad ECD antibody binding to migrating leader (L) and follower (F) cells. Scale bars, 10 μm. (I) Model diagram: YAP1 activation regulated by cell density affects N-cad surface expression and stimulates migration in neurons and glia but inhibits migration in ECM.

(C, D) Unpaired *t*-test. (F) Two-way ANOVA Šídák's multiple comparisons test. (H) Two-way ANOVA Tukey's multiple comparisons test. **P*<0.05, ** *P*<0.01, ****P*<0.001, *****P*<0.0001. ns, not significant. (C, D) N=30 cells. (F) N=5 experiments. (H) N=4 experiments.